Passivity-Based Partial Sequential Model Predictive Control of T-Type Grid-Connected Converters With Dynamic Damping Injection

Bo Long, *Senior Member, IEEE*, DaWei Shen, TianXu Cao, Jose Rodriguez, *Fellow, IEEE*, Josep M. Guerrero, *Fellow, IEEE*, Kil To Chong, *Member, IEEE*, and YunLong Teng

***Abstract*—*LCL*-filter interfaced three-level T-type converters have been widely used in low-voltage applications due to their elevated power quality. However, there exist several problems. To begin with, the performance of the finite-control-set model predictive control (FCS-MPC) controlled 3LT^{2}C relies on an accurate system model and measurement. Consequently, output performances will be influenced when model parameter mismatches, grid impedance variation, and the dead-time of power devices occur. In addition, the robustness of the FCS-MPC controller may also encounter challenges under disturbances and noise. Furthermore, *LCL*-filter has the resonance problems in the grid currents, which may endanger the system stability. To solve these problems, a passivity-based partial sequential MPC (PSMPC) with dynamic-damping injection method, which outperforms FCS-MPC and ensures the asymptotic stability, is proposed. First, the passive output voltage based on the Euler–Lagrange model is obtained using dynamic damping injection. Second, by embedding passive output voltage into MPC, a passivity-based PSMPC robust controller is designed to enhance its anti-disturbance abilities and achieve resonance suppression. Finally, to avoid the time-consuming of weighting factor selection, a PSMPC that allocates nonconflicting objectives in the same layer is introduced. Experimental results on 10-kW prototype demonstrates its excellent performance over existing techniques.**

***Index Terms*—Passivity-based control, sequential-model predictive control, three-level T-type converter.**

Manuscript received 27 November 2022; revised 4 March 2023; accepted 10 April 2023. Date of publication 12 April 2023; date of current version 19 May 2023. This work was supported in part by the Fundamental Research Funds for the Central Universities of China under Grant ZYGX2019J033, in part by the Natural Science Foundation of Sichuan Province under Grant 23NSFSC0294, in part by the Key Laboratory of Special Machine and High Voltage Apparatus, Shenyang University of Technology, Ministry of Education under Grant KFKT202206, in part by the Guangdong Basic and Applied Basic Research Foundation under Grant 2021A1515010666, and in part by the VELUX FOUNDATIONS under the VILLUM Investigator Grant Center for Research on Microgrids under Grant 25920. Recommended for publication by Associate Editor D. Dujic. *(Corresponding author: YunLong Teng.)*

Bo Long, DaWei Shen, and TianXu Cao are with the School of Mechanical and Electrical Engineering, Institute for Electric Vehicle Driving System and Safety Technology, University of Electronic Science and Technology of China, ChengDu 611731, China, also with the Yangtze Delta Region Institute (Huzhou), University of Electronic Science and Technology of China, Huzhou 313001, China, and also with the Institute of Electronic and Information Engineering, University of Electronic Science and Technology of China, Guangdong 523808, China (e-mail: longbouestc1980@126.com; shendaweii@163.com; caotxuestc@163.com).

Jose Rodriguez is with the Faculty of Engineering, Universidad Andres Bello, Santiago 8370146, Chile (e-mail: jose.rodriguez@unab.cl).

Josep M. Guerrero is with the Department of Energy Technology, Aalborg University, DK-9220 Aalborg, Denmark (e-mail: joz@et.aau.dk).

Kil To Chong is with the Department of Electronics and Information Engineering, Jeonbuk National University, Jeonju 54896, South Korea (e-mail: kitchong@jbnu.ac.kr).

YunLong Teng is with the School of Mechanical and Electrical Engineering, University of Electronic Science and Technology of China, ChengDu 611731, China (e-mail: ylteng@uestc.edu.cn).

Color versions of one or more figures in this article are available at https://doi.org/10.1109/TPEL.2023.3266588.

Digital Object Identifier 10.1109/TPEL.2023.3266588

NOMENCLATURE

$V_{\rm dc}$	dc-link voltage.
$C_{\rm dc}$	dc-bus capacitor.
$v_p,\ v_n$	Voltage of the upper- and lower-side dc-link capacitors.
u_a, u_b, u_c	Switching state of phase-a, b, and c.
v_N ,v_g	Converter-side and grid voltage.
$\boldsymbol{i}_1,\ \boldsymbol{i}_2, \boldsymbol{v_c}$	Converter-side current, grid current, and filter capacitor voltage.
$v_N^{\rm PBC}$, $v_N^{\rm con}$	Converter-side voltage with and without PBC control.
R_1, L_1	Resistance and inductance of Converter-side inductor.
C_f, v_C	Filter capacitance and its voltage.
L_2	Grid-side inductance.
k_d	Droop coefficient.
$e_{i_1},\ e_{i_2}$	Tracking error of i_1 , i_2.
$\boldsymbol{i}_{a,b,c}$	Three-phase grid current in *abc*-frame.
$\boldsymbol{v}_{a,b,c}$	Three-phase grid voltage in *abc*-frame.
$i_o(t)$, $i_{\rm dc}(t)$	NP current.
Δv_{np}	NP voltage difference.
$i_{1a},\ i_{1b}$, i_{1c}	Converter-side current of phase-a, b, and c.
T_s	Sampling time.
$u(k)$	Switching sequence of the power transistors at time instant k
$f_{\rm res}$	Resonance frequency of the *LCL*-filter.
$v_{N\alpha}, v_{N\beta}$	Converter-side voltage under the $\alpha\beta$ stationary frame.
$v_{g\alpha}, v_{g\beta}$	Grid-voltage under the $\alpha\beta$ stationary frame.
$\boldsymbol{R}_x$	Damping matrix.

I. INTRODUCTION

WITH increasing proportion of distributed generation, grid-connected converters (GCCs) play an increasingly crucial role in energy conversion. Compared to two-level topologies, three-level converters have been widely used in low- and

medium-voltage fields owing to their superior output voltage qualities and current advantages [1], [2]. Among several existing three-level converter structures (e.g., diode-clamp and flying-capacitor based three-level inverters), three-level T-type converters ($3LT^2C$) have been widely studied because of their unique advantages (with fewer switching elements and higher efficiency [3], [4]). The output current of $3LT^2C$ converter contains excess switching harmonics.

Recent literature shows that there are two main ways to overcome resonance. The first is to include a physical resistance to damp the resonance [9], [10]. However, this may incur additional costs and power loss. The second, active damping (AD), employs control algorithms for resonance suppression. In [5], Saïd-Romdhane et al. designed an AD of proportional-integral control for *LCL*-GCCs, which ensured the system stability under grid inductance variations. In [11], proportion-resonant control based on AD was used to overcome the resonant peak. To deal with the conflict between resonance suppression and harmonic-current amplification, Zhou et al. used inverter-side current feedback control in [12], which eliminated additional sensors. Based on offshore wind farm applications, in [13], the control stability for internal and external resonances was analyzed. Although the above methods can effectively overcome the resonant peak, $3LT^2C$ control requires a multiobjective optimization problem (MOOP) [e.g., output current quality and neutral-point (NP) voltage balance]. If other control objectives are used for optimizing, the controller design will become more complicated. On the contrary, model predictive control (MPC) can deal with MOOP simply by putting objectives into a cost function.

Recently, MPC has been widely used owing to its multiobjective optimization and good dynamic response [14], [15], [16]. In [17] and [18], a dual-vector MPC controller is proposed to minimize the total-harmonic-distortion (THD) of a single-phase NP-clamped pulsewidth modulated rectifier and to provide inertial support to a microgrid. However, it could achieve good robust under disturbances. For *LCL*-GCCs, in [19], the converter-side current, grid-side current, and filter capacitance voltage were used as the optimization objectives to ensure the system stability. However, the introduction of new feedback variables led to an increased number of weighting factors, thereby complicating their selection. In [20], the grid harmonic was solved by designing a hybrid cost function, although calculating the modified reference was complex. In [21], the power quality performance with different state feedback was selected as control objective in *LCL*-GCCs.

Although MPC is an embodiment of a simple multiobjective control, some inherent problems must be discussed. First, MPC implementation relies heavily on an accurate system model. Consequently, when internal parameters change or external disturbances occur, the control performance of the MPC considerably deteriorates, hampering the tracking of the control targets. To tackle the disturbance, an observer is usually used to compensate the accuracy of the model in MPC. In [22], a disturbance observer based on Extended-Kalman-Filter (EKF) was used to improve the system robustness. In this method, the grid voltage was calculated using EKF observer and the performance was guaranteed under a weak grid to eliminate internal disturbances (e.g., model parameter mismatch) in the system. In [23], [24], and [25], an extended-state observer (ESO) was designed to solve the model's sensitivity-related problems. However, the tuning parameters of ESO ought to have been determined. Recently, active disturbance rejection control was successfully introduced into MPC, thereby enhancing the disturbance rejection capability of the system [26], [27]. However, the additional nonlinear observer was introduced and multiple parameters needed to be adjusted.

Second, traditional MPCs need to predetermine the weighting factors, which are time-consuming and require repeated experiments [28], [29], [30]. To solve this problem, sequential model predictive control (SMPC) was proposed to achieve MOOP by controlling the targets layer by layer [31]. However, in conventional SMPC, the number of candidates in each layer should be determined in advance, while each control object is allocated to a single layer, which may cause sub-optimization problems [32].

Recently, passivity-based control (PBC) was introduced to improve the system stability and enhance its anti-disturbance ability [33], [34]. Passivity-based control directly correlates the state variables with the system energy, ensuring the convergence of the energy storage function by means of damping injection and power sharing. In [35], PBC was used for power decoupling control regarding power quality improvement. In [36], PBC was used to attenuate the influence of the time-delay in inverter control.

From the above research, although MPC can directly solve the MOOP of *LCL*-GCCs, its robustness remains poor. During normal operations with MPC, owing to the aging phenomenon and increase in ambient temperature, the filter parameters may deviate from their desired values. Consequently, the model mismatches and the dead-time of power device (also regarded as internal disturbance) may lead to serious grid current distortion. In addition, when external disturbances (e.g., grid voltage distortion, voltage-drop) occur, MPC recovery is inadequate, leading to an unstable system. Contrarily, PBC is robust to system parameter variations and external perturbations from the perspective of energy dissipation. Considering the merits of MPCs and PBCs, a novel method called DDPB-PSMPC is proposed herein. First, a dynamic damping injection strategy is proposed to improve the input in the PBC. Based on the prediction idea, the tracking error of the converter-side current in a future instance is extrapolated and calculated. Furthermore, the injected damping was determined following the average prediction error. Second, based on the Euler–Lagrange (EL) model of *LCL*-$3LT^2C$, the converter voltage of PBC is calculated and sent to the predictive controller as a reference. Finally, considering the output performance and weight factor design, a new partial SMPC (PSMPC), which groups the nonconflicting objectives into the same layer, is proposed to optimize the control objectives.

In summary, the main contributions of this study are as follows:

1) Based on the prediction error, a novel PBC (DDPB) method using dynamic damping injection is proposed.

This proposed method can adjust the injected damping in real-time following the prediction error, which considers both the convergence time and steady-state error of the system.

2) The output voltage, which was based on the DDPB method, fed the predictive control as a reference to optimize the converter voltage. By embedding DDPB into the MPC, the system has less steady-state error and is more robust to parameter variations, noise, and external perturbations.
3) To reduce the weighting factors and control objectives, a new PSMPC that places nonconflicting objectives in same layers is introduced. By using DDPB-PSMPC, the system can maintain an excellent output and avoid suboptimal problems caused by sequential optimization.
4) In the proposed DDPB-PSMPC method, the harmonic resonance is successfully suppressed by converter-side voltage control without including additional control objectives.

The rest of this article is organized as follows: In Section II, the modeling of *LCL*-3LT^{2}C GCC is presented. A prediction equation was established and the inherent problems of *LCL*-3LT^{2}C were introduced. Section III presents the fundamental PBC using the EL model and demonstrates the passivity of the system. Moreover, the impact of the damping matrix on system stability is also analyzed. In Section IV, a preliminary MPC for *LCL*-3LT^{2}C is introduced. In Section V, passivity-based PSMPC control and its implementation are presented. To verify the effectiveness of the DDPB-PSMPC, experimental results under different scenarios are presented in Section VI. Finally, Section VII concludes this article and provides suggestions for future research.

II. Modeling and Problem Description of 3LT^{2}C GCCs With *LCL*-Filter

From this section, we first introduce the discrete prediction model of *LCL*-3LT^{2}C grid-connected converter, which is the based for PMPC, then the discrete model of DDPB controller will be introduced. Finally, the combination of DDPB and partial SMPC controllers are introduced. The output voltage of DDPB derived by EL model is embedded into the cost function of PSMPC to achieve strong system robustness with smaller steady-state errors, which inherits the advantages of two control methods.

A. Topology Description

The topology of the *LCL*-3LT^{2}C grid-connected converter is illustrated in Fig. 1. $V_{\rm dc}$ is the dc-link voltage. The dc-bus side uses two series capacitors $C_{\rm dc}$ to divide the high voltage. The voltages of the two capacitors are v_p and v_n, respectively, where P and N represent the positive and negative poles of the dc bus, respectively. Each phase of *LCL*-3LT^{2}C consisted of four switching elements: T_{i1}, T_{i2}, T_{i3}, and T_{i4} $(i = a, b, c)$. T_{i1} and T_{i4} are vertical switches, while T_{i2} and T_{i3} are horizontal switches for midpoint clamping. An active damping technique was used to reduce additional power losses.

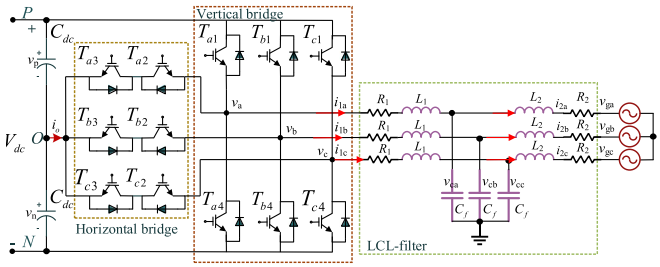

Fig. 1. Topology of the 3LT^{2}C GCC with an *LCL*-filter.

TABLE I
Output of the 3LT^{2}C Converter

Switching state	V_{out}	T_{i1}	T_{i2}	T_{i3}	T_{i4}
1	$0.5V_{dc}$	on	on	off	off
0	0	off	on	on	off
-1	$-0.5V_{dc}$	off	off	on	on

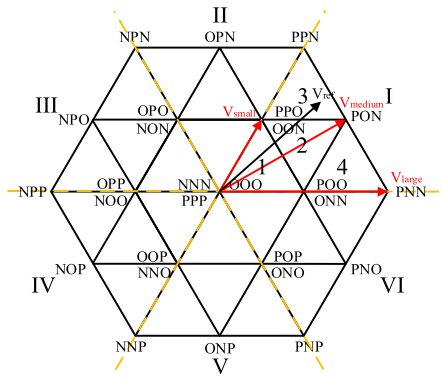

Fig. 2. Space voltage vectors of the three-phase T-type converter.

According to different switching state, the output voltage is given Table I.

B. Modeling of LCL-3LT^{2}C Converter

As shown in Fig. 1, the 3LT^{2}C consists of NP switches and vertical half-bridge switches, followed by an *LCL*-filter. In each phase of the three-level converter, there are three switching states: [P], [O], and [N]. Thus, the 3LT^{2}C has totally 27 switching state combinations. These switching states can be represented by space voltage vectors, which can be divided into four groups based on their magnitudes: zero-, small-, medium-, and large-voltage vectors.

The space voltage vectors of the T-type three-level converter are shown in Fig. 2. The vector space is divided into six large sectors, namely I, II, III, IV, V, and VI, and each large sector is divided into four small sectors, namely, 1, 2, 3, and 4 (see Fig. 2).

To establish the mathematical model of *LCL*-3LT^{2}C, the switching vector is defined as follows:

$$\boldsymbol{u} = [u_a, u_b, u_c]^T. \tag{1}$$

According to Table I, u_a, u_b, u_c can be $[-10, 1]$. Assuming the two dc-link capacitor voltage V_p and V_n are balanced, namely, $V_{\mathrm{p}}{=}V_n$, the relationship between the converter-side voltage $\boldsymbol{v}_N^{\mathrm{con}}$ and dc-link voltage V_{dc} can be expressed as follows:

$$\boldsymbol{v}_N^{\mathrm{con}} = \frac{V_{\mathrm{dc}}}{2}\,\boldsymbol{u} \tag{2}$$

In practice, the voltage of the two dc-link capacitors may not be equal, to solve this problem, the balance control of neutral-point voltage is arranged in the first layer (highest priority) of sequential model predictive control, which will be discussed in the subsequent sections. According to Kirchhoff's law, the current and voltage equations of *LCL*-3LT^{2}C can be derived as follows:

$$\begin{cases} \frac{d\boldsymbol{i}_1}{dt} = -\frac{R_1}{L_1}\boldsymbol{i}_1 - \frac{1}{L_1}\boldsymbol{v}_C + \frac{1}{L_1}\boldsymbol{v}_N^{\mathrm{con}} \\ \frac{d\boldsymbol{i}_2}{dt} = -\frac{R_2}{L_2}\boldsymbol{i}_2 + \frac{1}{L_2}\boldsymbol{v}_C - \frac{1}{L_2}\boldsymbol{v}_{\mathrm{PCC}} \\ \frac{d\boldsymbol{v}_C}{dt} = \frac{1}{C_f}\,\boldsymbol{i}_1 - \frac{1}{C_f}\boldsymbol{i}_2 \end{cases} \tag{3}$$

where $\boldsymbol{i}_1$, $\boldsymbol{i}_2$, $\boldsymbol{v}_c$, and $\boldsymbol{v}_g$ are the converter-side current, grid current, filter capacitor voltage, and grid voltage, respectively. The above three-phase vectors are defined as follows:

$$\begin{cases} \boldsymbol{i}_1(t) = [\boldsymbol{i}_{1a}, \boldsymbol{i}_{1b}, \boldsymbol{i}_{1c}]^T \\ \boldsymbol{i}_2(t) = [\boldsymbol{i}_{2a}, \boldsymbol{i}_{2b}, \boldsymbol{i}_{2c}]^T \\ \boldsymbol{v}_c(t) = [\boldsymbol{v}_{ca}, \boldsymbol{v}_{cb}, \boldsymbol{v}_{cc}]^T \\ \boldsymbol{v}_{\mathrm{PCC}}(t) = [\boldsymbol{v}_{\mathrm{PCC}_a}, \boldsymbol{v}_{\mathrm{PCC}_b}, \boldsymbol{v}_{\mathrm{PCC}_c}]^T. \end{cases} \tag{4}$$

To simplify the equations, the three-phase vectors can be transformed to $\alpha\beta0$ stationary frame by Clarke transformation, given as follows:

$$\begin{cases} \boldsymbol{i}_{1\alpha\beta}\,(t) = \boldsymbol{K}_{3s/2s}\,\boldsymbol{i}_1\,(t) \\ \boldsymbol{i}_{2\alpha\beta}\,(t) = \boldsymbol{K}_{3s/2s}\,\boldsymbol{i}_2\,(t) \\ \boldsymbol{v}_{c\alpha\beta}\,(t) = \boldsymbol{K}_{3s/2s}\,v_c\,(t) \\ \boldsymbol{v}_{\mathrm{PCC}\alpha\beta}\,(t) = \boldsymbol{K}_{3s/2s}\,v_{\mathrm{PCC}}\,(t) \end{cases} \tag{5}$$

where $\boldsymbol{K}_{3s/2s}$ represents the Clarke transformation matrix which is defined as follows:

$$\boldsymbol{K}_{3s/2s} = \frac{2}{3}\begin{bmatrix} 1 & -\frac{1}{2} & -\frac{1}{2} \\ 0 & \frac{\sqrt{3}}{2} & -\frac{\sqrt{3}}{2} \end{bmatrix}.$$

In the $\alpha\beta0$ coordinate system, the state variable matrix is selected as $\boldsymbol{x}(t) = [i_{1\alpha\beta}, i_{2\alpha\beta}, v_{c\alpha\beta}]^T$, and the continuous-time state equation and output equation are described as follows:

$$\begin{cases} \dot{\boldsymbol{x}}\,(t) = \boldsymbol{F}x\,(t) + \boldsymbol{G}u\,(t) + \boldsymbol{P}v_{\mathrm{PCC}}\,(t) \\ \boldsymbol{y}\,(t) = \boldsymbol{C}x\,(t) \end{cases} \tag{6}$$

where state variable matrix $\boldsymbol{F}$, input control matrix $\boldsymbol{G}$, disturbance matrix $\boldsymbol{P}$, and output control matrix $\boldsymbol{C}$ in (6) are expressed as follows:

$$\boldsymbol{F} = \begin{bmatrix} \frac{R_1}{-L_1}\cdot\boldsymbol{I}_{2\times2} & \boldsymbol{O}_{2\times2} & \frac{1}{-L_1}\cdot\boldsymbol{I}_{2\times2} \\ \boldsymbol{O}_{2\times2} & \frac{R_2}{-L_2}\cdot\boldsymbol{I}_{2\times2} & \frac{1}{L_2}\cdot\boldsymbol{I}_{2\times2} \\ \frac{1}{C_f}\cdot\boldsymbol{I}_{2\times2} & \frac{1}{-C_f}\cdot\boldsymbol{I}_{2\times2} & \boldsymbol{O}_{2\times2} \end{bmatrix},$$

$$\boldsymbol{G} = \begin{bmatrix} \frac{V_D}{2L_1}\cdot\boldsymbol{I}_{2\times2} & \boldsymbol{O}_{2\times2} & \boldsymbol{O}_{2\times2} \end{bmatrix}^{\boldsymbol{T}} \boldsymbol{K}_{3s/2s},$$

$$\boldsymbol{P} = \begin{bmatrix} \boldsymbol{O}_{2\times2} & -\frac{1}{L_2}\cdot\boldsymbol{I}_{2\times2} & \boldsymbol{O}_{2\times2} \end{bmatrix}^T \boldsymbol{K}_{3s/2s},$$

$$\boldsymbol{C} = \begin{bmatrix} \boldsymbol{I}_{2\times2} & \boldsymbol{O}_{2\times2} & \boldsymbol{O}_{2\times2} \\ \boldsymbol{O}_{2\times2} & \boldsymbol{I}_{2\times2} & \boldsymbol{O}_{2\times2} \\ \boldsymbol{O}_{2\times2} & \boldsymbol{O}_{2\times2} & \boldsymbol{O}_{2\times2} \end{bmatrix}.$$

From (6) and matrix $\boldsymbol{C}$, the output vector $\mathbf{y}$ are the output currents of the converter-side and grid-side inductors needed to be controlled. Using the Du Hamel formula [37] to discretize (6), the discrete-time prediction model can be expressed as follows:

$$\begin{cases} \boldsymbol{x}\,(k+1) = \boldsymbol{A}\boldsymbol{x}\,(k) + \boldsymbol{B}\boldsymbol{u}\,(k) + \boldsymbol{T}\boldsymbol{v}_{\boldsymbol{g}}\,(k) \\ \boldsymbol{y}\,(k+1) = \boldsymbol{C}\boldsymbol{x}\,(k+1) \end{cases} \tag{7}$$

where $\boldsymbol{A} = \boldsymbol{e}^{\boldsymbol{F}\boldsymbol{T}_{\boldsymbol{s}}}$, $\boldsymbol{B} = -\boldsymbol{F}^{-1}(\boldsymbol{I}-\boldsymbol{A})\boldsymbol{G}$, $\boldsymbol{T} = -\boldsymbol{F}^{-1}(\boldsymbol{I}-\boldsymbol{A})\boldsymbol{P}$.

C. Modeling of Neutral-Point Current

In Fig. 1, the capacitor voltages V_{p} and V_{n} are controlled by the currents that flow in and draw out. When the $\mathrm{V_{dc}}$ is provided by direct-current (dc) voltage source, the only element that affects the capacitor voltage is the neutral point current i_{o}. Because of the possible mismatch between the capacitors' voltages, V_p may not be equal to V_n, the dc-link capacitor voltage difference Δv_{np} can be expressed as follows [38]:

$$C_{\mathrm{dc}}\frac{d}{dt}\Delta V_{np} = C_{\mathrm{dc}}\frac{d}{dt}\left(V_{\mathrm{p}} - V_{\mathrm{n}}\right) = i_o = -i_{1abc}^T \cdot \mathrm{abs}(\boldsymbol{u}) \tag{8}$$

where $i_{1abc} = \begin{bmatrix} i_{1a} & i_{1b} & i_{1c} \end{bmatrix}^T$ is the three-phase converter-side current in the abc frame and abs $(\mathbf{u}) = \begin{bmatrix} |u_a| & |u_b| & |u_c| \end{bmatrix}^T$.

D. Problem Description

1) Neutral-Point Voltage: 3LT^{2}C faces NP voltage fluctuations ($v_p \neq v_n$). When the NP voltage is unbalanced, both series capacitors encounter unbalanced charging and discharging processes. Hence, it is important to control the NP voltage difference caused by NP current $i_o(t)$, the relationship between Δv_{np} and $i_o(t)$ can be written as follows:

$$-\frac{d}{dt}\Delta v_{np}\,(t) = \frac{1}{C_{\mathrm{dc}}}\,i_o\,(t)\,. \tag{9}$$

The relationship between $i_o(t)$ and the switching vector $\boldsymbol{u}$ can be established as follows:

$$i_o\,(t) = (1-|u_a|)\,i_{1a} + (1-|u_b|)\,i_{1b} + (1-|u_c|)\,i_{1c}. \tag{10}$$

The three-phase system are symmetrical, indicating that $i_{1a} + i_{1b} + i_{1c} = 0$. Consequently, $i_o(t)$ can be rewritten as follows:

$$-i_o\,(t) = |u_a|\;i_{1a}\,(t) + |u_b|\,i_{1b}\,(t) + |u_c|\,i_{1c}\,(t)\,. \tag{11}$$

Substituting (11) into (9), the relationship between Δv_{dc} and $i_o(t)$ can be rewritten as follows:

$$\frac{d}{dt}\Delta v_{np}\,(t) = \frac{1}{C_{\mathrm{dc}}}\;\left(|u_a|\,i_{1a}\,(t) + |u_b|\,i_{1b}\,(t) + |u_c|\,i_{1c}\,(t)\right). \tag{12}$$

Equation (12) was discretized using the Euler forward method and the prediction model of NP voltage difference can be expressed as follows:

$$\Delta v_{np}(k+1) = \frac{T_s}{C_{\text{dc}}} |\boldsymbol{u}(k)|^T i_1(k) + \Delta v_{np}(k) \tag{13}$$

where T_s represents the sampling time and $\boldsymbol{u}(k)$ represents the switching sequence of the power transistors at time instant k.

2) Resonance of an LCL*-Filter:* The *LCL*-filter has an attenuation rate of -60 dB in high-frequency range, which can eliminate high-order harmonics of the switching power converters and ensure high-quality integration of the grid current. However, a resonance peak may destabilize the system. The resonant frequency f_{res} can be expressed as follows [9], [10]:

$$\omega_{\text{res}} = \sqrt{\frac{L_1 + L_2}{L_1 L_2 C_f}}, f_{\text{res}} = \frac{\omega_{\text{res}}}{2\pi}. \tag{14}$$

Equation (14) shows that the grid current is easily resonated because of the peak at the natural resonance frequency [ω_{res} expressed in (14)] [39], [40]. The state variables related to the *LCL*-filter are inverter current i_1, filter capacitor voltage v_c, and grid current i_2. The high-frequency component of these state variables is the excitation source for the resonance problem. Thus, the AD algorithm usually dampens the resonance by introducing the state feedback control from these state variables, which does not need any additional hardware components.

III. Passivity-Based Control

A. Preliminaries of PBC Theory

The PBC associates the state variables of the system with energy. The PBC seeks the energy storage function $E(x)$ and calculated $E(X_0)$ (X_0 is the expected equilibrium point of the system), thus global stability and output performance are achieved by converging $E(x)$ to $E(X_0)$. The designing of the PBC is involved in two steps, i.e., power shaping and damping injection. Many systems, which do not contain energy sources, can be described by the EL equation. Since there is no energy source in *LCL*-3LT^{2}C, its EL model is established.

Selecting $\boldsymbol{i} = [v_{N\alpha}^{\text{PBC}}, v_{N\beta}^{\text{PBC}}, -\boldsymbol{v}_{\text{PCC}\alpha}, -\boldsymbol{v}_{\text{PCC}\beta}, 00]^T$ as the input vector, $v_{N\alpha}^{\text{PBC}}$ and $v_{N\alpha}^{\text{PBC}}$ are the converter-side voltage which are passive, $v_{g\alpha}$ and $\boldsymbol{v}_{g\beta}$ are the grid voltage. The EL model of *LCL*-3LT^{2}C can be expressed as follows:

$$\boldsymbol{M}\dot{\boldsymbol{x}} + \boldsymbol{J}\boldsymbol{x} + \boldsymbol{R}\boldsymbol{x} = \boldsymbol{i} \tag{15}$$

where $\boldsymbol{M}$ and $\boldsymbol{R}$ are the positive-definite symmetric matrices that reflect the energy storage and dissipation situations of the system, respectively. $\boldsymbol{J}$is a skew-symmetric matrix ($\boldsymbol{J} = -\boldsymbol{J}^T$), which reflects the couplings within the system. $\boldsymbol{x}$ is the system variable. Here, $\boldsymbol{M}$, $\boldsymbol{R}$, and $\boldsymbol{J}$are expressed as follows:

$$\begin{aligned}\boldsymbol{M}_{6\times6} &= \text{diag}\left[L_1, L_1, L_2, L_2, C_f, C_f\right], \boldsymbol{R}_{6\times6} \\ &= \text{diag}\left[R_1, R_1, R_2, R_2, 0, 0\right] \\ \boldsymbol{J}_{6\times6} &= \begin{bmatrix} O_{2\times2} & O_{2\times2} & I_{2\times2} \\ O_{2\times2} & O_{2\times2} & -I_{2\times2} \\ -I_{2\times2} & I_{2\times2} & O_{2\times2} \end{bmatrix}.\end{aligned}$$

Defining the error matrix $\boldsymbol{x}_e = \boldsymbol{x}^* - \boldsymbol{x}$, the EL model of *LCL*-3LT^{2}C based on error analysis can be expressed as follows:

$$\begin{aligned}&\underbrace{\boldsymbol{M}}_{6\times6}\underbrace{\dot{\boldsymbol{x}}_e}_{6\times1} + \underbrace{\boldsymbol{J}}_{6\times6}\underbrace{\boldsymbol{x}_e}_{6\times1} + \underbrace{\boldsymbol{R}}_{6\times6}\boldsymbol{x}_e \\ &= \boldsymbol{M}\underbrace{\dot{\boldsymbol{x}}^*}_{6\times1} + \boldsymbol{J}\underbrace{\boldsymbol{x}^*}_{6\times1} + \boldsymbol{R}\boldsymbol{x}^* - \underbrace{\boldsymbol{i}}_{6\times1}.\end{aligned} \tag{16}$$

The error energy function is selected as $E = 0.5\boldsymbol{x}_e^T\boldsymbol{M}\boldsymbol{x}_e$, to ensure that the state variable reaches the desired equilibrium point and the system should satisfy the following constraints:

$$\boldsymbol{x}_e \to 0,\ E \to 0,\ \dot{E} \le 0. \tag{17}$$

To ensure that *LCL*-3LT^{2}C satisfies (17), it is important to inject damping so that it rapidly attains the reference state variable. The injection-damping term is expressed as follows:

$$(\boldsymbol{R} + \boldsymbol{R}_x)\boldsymbol{x}_e = \boldsymbol{R}_d\boldsymbol{x}_e \tag{18}$$

where $\boldsymbol{R}_{\boldsymbol{x}}$ is the damping matrix, and $\boldsymbol{R}_{\boldsymbol{x}} =$ diag$[r_{x1}, r_{x1}, r_{x2}, r_{x2}, r_{x3}, r_{x3}]_{6\times6}$, substituting (18) for (16), the EL model of 3LT^{2}C can be rewritten as follows:

$$\boldsymbol{M}\dot{\boldsymbol{x}}_e + \boldsymbol{J}\boldsymbol{x}_e + \boldsymbol{R}_d\boldsymbol{x}_e = \boldsymbol{M}\dot{\boldsymbol{x}}^* + \boldsymbol{J}\boldsymbol{x}^* + \boldsymbol{R}\boldsymbol{x}^* - \boldsymbol{i} + \boldsymbol{R}_X\boldsymbol{x}_e. \tag{19}$$

To guarantee the system stability, the left term of (19) should attain zero. Thus, the input vector $\boldsymbol{i}$ and $\dot{E}(x)$ can be calculated as follows:

$$\begin{cases} \boldsymbol{i} = \boldsymbol{M}\dot{\boldsymbol{x}}^* + \boldsymbol{J}\boldsymbol{x}^* + \boldsymbol{R}\boldsymbol{x}^* + \boldsymbol{R}_X\boldsymbol{x}_e & (a) \\ \dot{E}(x) = -\boldsymbol{x}_e^T(\boldsymbol{R} + \boldsymbol{R}_x)\boldsymbol{x}_e = -\boldsymbol{x}_e^T\boldsymbol{R}_d\boldsymbol{x}_e \le 0 & (b). \end{cases} \tag{20}$$

This indicates that the convergence speed of the system is related with the injected damping $\boldsymbol{R}_X$. Consequently, (20.a) provides the passive input of PBC for *LCL*-3LT^{2}C and the switching signal based on (20) can improve both the power quality of the grid current and system robustness. It is needed to note that the input i guarantees the passivity of the 3LT^{2}C converter. Considering *LCL*-filter is a passive network, thereby, according to the passivity characteristic theorem, when two passive circuit networks are series connected, the while system would also be passive.

For digital implementation, the discrete model of (20) with the sampling time T_s by backward Euler can be derived

$$\boldsymbol{i}(k) = \boldsymbol{M}\frac{\boldsymbol{x}^*(k) - \boldsymbol{x}^*(k-1)}{T_s} + \boldsymbol{J}\boldsymbol{x}^*(k) + \boldsymbol{R}\boldsymbol{x}^*(k) + \boldsymbol{R}_X\boldsymbol{x}_e(k) \tag{21}$$

where $\boldsymbol{x}_e(k) = \boldsymbol{x}^*(k) - \boldsymbol{x}(k)$.

B. Passivity Analysis of 3LT^{2}C Converter

If the PBC controller is used in the 3LT^{2}C, it must be guaranteed that the inverter is strictly passive. In other words, the energy stored inside the *LCL*-3LT^{2}C inverter should not be greater than the energy supplied to the inverter at any given

time. The following formula should be satisfied:

$$H(\boldsymbol{x}(T)) - H(\boldsymbol{x}(0)) \leq \int_0^T u^T y d\tau - \int_0^T Q(x) d\tau, T > 0 \tag{22}$$

$$\text{Or} \quad \dot{H}(\boldsymbol{x}) \leq \boldsymbol{u}^T \boldsymbol{y} - Q(\boldsymbol{x}) \tag{23}$$

where $x(t)$, $u(t)$, and $y(t)$ represent the system state, input, and output vectors, respectively, $H(\boldsymbol{x}(T)) - H(\boldsymbol{x}(0))$ represents the energy stored inside the 3LT^{2}C, $\int_0^T u^T y d\tau$ represents the external energy supplied to the inverter , and $\int_0^T Q(\boldsymbol{x}) d\tau$ represents the total dissipated energy in the 3LT^{2}C.

If the 3LT^{2}C converter is passive, it must be internal stable, thus the dissipated energy will make the stable variable $\boldsymbol{x}(t)$ converge to the desired equilibrium point. The term here is used to describe the dynamics of the control system

$$\begin{aligned} & L_1 i_{1\alpha} \frac{di_{1\alpha}}{dt} + L_1 i_{1\beta} \frac{di_{1\beta}}{dt} + L_2 i_{2\alpha} \frac{di_{2\alpha}}{dt} + L_2 i_{2\beta} \frac{di_{2\beta}}{dt} \\ & + \frac{1}{2} \mathrm{c}_f \left(v_{c\alpha}^2 + v_{c\beta}^2 \right) \\ & = u_{\mathrm{dc}} i_{\mathrm{dc}} - v_{\mathrm{PCC}\alpha} i_{2\alpha} - v_{\mathrm{PCC}\beta} i_{2\beta} \\ & - (i_{1\alpha}^2 + i_{1\beta}^2) R_1 - (i_{2\alpha}^2 + i_{2\beta}^2) R_2. \end{aligned} \tag{24}$$

Then, (24) can be written as follows:

$$\begin{aligned} & \frac{d}{dt} \left(\frac{L_1 (i_{1\alpha}^2 + i_{1\beta}^2)}{2} + \frac{L_2 (i_{2\alpha}^2 + i_{2\beta}^2)}{2} \right) + \frac{1}{2} \mathrm{c}_f \left(v_{c\alpha}^2 + v_{c\beta}^2 \right) \\ & = u_{\mathrm{dc}} i_{\mathrm{dc}} - (v_{\mathrm{PCC}\alpha} i_{2\alpha} + v_{\mathrm{PCC}\beta} i_{2\beta}) \\ & - (i_{1\alpha}^2 + i_{1\beta}^2) R_1 - (i_{2\alpha}^2 + i_{2\beta}^2) R_2 \end{aligned} \tag{25}$$

when define $H(x)$, $u^{\mathrm{T}}y$, and $Q(x)$ as

$$H(x) = \frac{L_1 (i_{1\alpha}^2 + i_{1\beta}^2)}{2} + \frac{L_2 (i_{2\alpha}^2 + i_{2\beta}^2)}{2} + \frac{1}{2} \mathrm{c}_f \left(v_{c\alpha}^2 + v_{c\beta}^2 \right)$$

$$\begin{aligned} u^T y &= u_{\mathrm{dc}} i_{\mathrm{dc}} - (v_{\mathrm{PCC}\alpha} i_{2\alpha} + v_{\mathrm{PCC}\beta} i_{2\beta}) Q(x) \\ &= (i_{1\alpha}^2 + i_{1\beta}^2) R_1 + (i_{2\alpha}^2 + i_{2\beta}^2) R_2 > 0. \end{aligned}$$

Based on the above analysis, the *LCL*-3LT^{2}C system is passive when implementing PBC controller. The key to implementing PBC control is that the passive input $\boldsymbol{i}$ can be strictly satisfied, since the elements $-\boldsymbol{v}_{\mathrm{PCC}\alpha\beta}$ and 0 cannot be controlled, so the followings will explain how to apply $\boldsymbol{i}$ and ensure that the components of $\boldsymbol{i}$ are equal to the theoretical calculation (20.a).

Defining vectors $\boldsymbol{v}_N^{\mathrm{PBC}} = [v_{Na}^{\mathrm{PBC}}, v_{Nb}^{\mathrm{PBC}}, v_{Nc}^{\mathrm{PBC}}]^T$ and $\boldsymbol{v}_{N\alpha\beta}^{\mathrm{PBC}} = [v_{N\alpha}^{\mathrm{PBC}}, v_{N\beta}^{\mathrm{PBC}}]^T$, then we have $\boldsymbol{v}_{N\alpha\beta}^{\mathrm{PBC}} = K_{3s/2s} \boldsymbol{v}_N^{PBC}$. According to (20.a), the passive input **i** is calculated as follows:

$$\begin{cases} \boldsymbol{v}_{N\alpha\beta}^{\mathrm{PBC}} = L_1 \frac{d\boldsymbol{i}_{1\alpha\beta}^*}{dt} + \boldsymbol{v}_{c\alpha\beta} + R_1 \boldsymbol{i}_{1\alpha\beta}^* + r_{x1\alpha\beta} (\boldsymbol{i}_{1\alpha\beta}^* - \boldsymbol{i}_{1\alpha\beta}) \\ -\boldsymbol{v}_{\mathrm{PCC}\alpha\beta} = L_2 \frac{d\boldsymbol{i}_{2\alpha\beta}^*}{dt} - \boldsymbol{v}_{c\alpha\beta} + R_2 \boldsymbol{i}_{2\alpha\beta}^* + r_{x2\alpha\beta} (\boldsymbol{i}_{2\alpha\beta}^* - \boldsymbol{i}_{2\alpha\beta}) \\ 0 = C_f \frac{d\boldsymbol{v}_{c\alpha\beta}^*}{dt} - \boldsymbol{i}_{1\alpha\beta}^* + \boldsymbol{i}_{2\alpha\beta}^* + r_{x3\alpha\beta} (\boldsymbol{v}_{c\alpha\beta}^* - \boldsymbol{v}_{c\alpha\beta}). \end{cases} \tag{26}$$

If six components of the vector $\boldsymbol{i}$are applied, then the *LCL*-3LT^{2}C system would be passive. For the elements $\boldsymbol{v}_{N\alpha\beta}^{PBC}$, it is possible to impose

$$\begin{cases} v_{N\alpha\beta}^{\mathrm{PBC}} = L_1 \frac{di_{1\alpha\beta}^*}{dt} + v_{c\alpha\beta}^* + R_1 i_{1\alpha\beta}^* + r_{x1\alpha\beta} \Delta i_{1\alpha\beta} \\ v_{N\alpha\beta}^{\mathrm{con}} = \frac{V_{\mathrm{dc}}}{2} \boldsymbol{K}_{3s/2s} \boldsymbol{u}. \end{cases} \tag{27}$$

As shown in (27), in the proposed method, $v_{N\alpha\beta}^{\mathrm{PBC}}$ is calculated according to DDPB algorithm, and then $v_{N\alpha\beta}^{\mathrm{PBC}}$ is regarded as the reference of $v_{N\alpha\beta}^{\mathrm{con}}$ in PSMPC. By controlling the switching vector, $v_{N\alpha\beta}^{\mathrm{PBC}}$ is tracked with $v_{N\alpha\beta}^{\mathrm{con}}$, so $v_{N\alpha\beta}^{\mathrm{PBC}}$ can be controlled.

As shown in (26), the injection damping term $r_{x1\alpha\beta}$ affects the calculation of v_N^{PBC}, setting $r_{x1\alpha} = r_{x1\beta} = r_{x1}$, the design of r_{x1} will be discussed in the next section, while $r_{x2\alpha\beta}$ and $r_{x3\alpha\beta}$ are independent of $v_{N\alpha\beta}^{\mathrm{PBC}}$. Therefore, when designing the dynamic damping rules, only r_{x1} is adjusted. In (26), $r_{x2\alpha\beta}$ and $r_{x3\alpha\beta}$ are not used for computing $v_{N\alpha\beta}^{\mathrm{PBC}}$ but related to the components of $\boldsymbol{i}$: $v_{\mathrm{PCC}\alpha\beta}$ and 0.

For $v_{\mathrm{PCC}\alpha\beta}$, the common-coupling-point voltage cannot be controlled. However, to guarantee the passivity of *LCL*-3LT^{2}C, $v_{\mathrm{PCC}\alpha}$ and $v_{\mathrm{PCC}\beta}$ should be equal to the values $\boldsymbol{i}$ [3] and $\boldsymbol{i}$ [4] ($v_{\mathrm{PCC}\alpha} = \boldsymbol{i}[3]$, $v_{\mathrm{PCC}\beta} = \boldsymbol{i}[4]$), and the following equations should be existed:

$$-v_{\mathrm{PCC}\alpha\beta} = L_2 \frac{d\boldsymbol{i}_{2\alpha\beta}^*}{dt} - \boldsymbol{v}_{c\alpha\beta}^* + R_2 \boldsymbol{i}_{2\alpha\beta}^* + r_{x2\alpha\beta} (\boldsymbol{i}_{2\alpha\beta}^* - \boldsymbol{i}_{2\alpha\beta}). \tag{28}$$

Although $v_{\mathrm{PCC}\alpha\beta}$ cannot be controlled, $r_{x2\alpha\beta}$ can be designed to ensure the left- and right-side of the equation are equal. After discretizing the assumption (28), $r_{x2\alpha\beta}$ can be calculated as follows:

With the $r_{x2\alpha\beta}$ in (29), the assumption (28) can be available, it should be noted that $i_{2\alpha\beta}^*(k) = i_{2\alpha\beta}(k)$ is the most ideal case of the *LCL*-3LT^{2}C system. At this time, $r_{x2\alpha\beta}$ can be set to 0, and the controller will not be affected.

As for the components $\boldsymbol{i}$ [5] and $\boldsymbol{i}$ [6], to guarantee the passivity of *LCL*-3LT^{2}C, $\boldsymbol{i}$ [5] and $\boldsymbol{i}$ [6] should be equal to 0. The assumption is listed as follows:

$$0 = C_f \frac{d\boldsymbol{v}_{c\alpha\beta}^*}{dt} - \boldsymbol{i}_{1\alpha\beta}^* + \boldsymbol{i}_{2\alpha\beta}^* + \mathbf{r}_{x3\alpha\beta} (\boldsymbol{v}_{c\alpha\beta}^* - \boldsymbol{v}_{c\alpha\beta}). \tag{30}$$

Similar to the derivation steps of (29), shown at the bottom of the next page. after discretizing (30), $r_{x3\alpha\beta}$ can be calculated as follows:

With the $r_{x3\alpha\beta}$ in (31) shown at the bottom of the next page, the assumption (30) can be available, it also should be noted that $\boldsymbol{v}_{c\alpha\beta}^*(k) = v_{c\alpha\beta}(k)$ is the most ideal case of the *LCL*-3LT^{2}C system. At this time, $r_{x3\alpha\beta}$ can be set to 0, and the controller will not be affected.

In summary, $v_{N\alpha\beta}^{\mathrm{PBC}}$ can be controlled by switching vectors, the assumption (28) and (30) be can realized by setting $r_{x2\alpha\beta}$, $r_{x3\alpha\beta}$ according to (29) and (31), as the result, the uncontrolled components $-\boldsymbol{v}_{\mathrm{PCC}\alpha}, -\boldsymbol{v}_{\mathrm{PCC}\beta}, 00$ can be equal to $\boldsymbol{i}$ [3], $\boldsymbol{i}$ [4], $\boldsymbol{i}$ [5], $\boldsymbol{i}$ [6], respectively. Then, passive input $\boldsymbol{i}$ can be applied completely. As a result, *LCL*-3LT^{2}C system is passive.

When the energy of the 3LT^{2}C satisfies (22) and passive input $\boldsymbol{i}$ can be strictly satisfied. The three-phase *LCL*-3LT^{2}C is strictly passive, and the PBC controller can be used.

C. Analysis of Damping Matrix $\boldsymbol{R_x}$

For PBC control, additional damping matrix $\boldsymbol{R}_x$ in (18) is injected to accelerate the convergence speed of the system and boost the system stability. In this section, the impact of $\boldsymbol{R}_x$ on the state variables is analyzed to assist in designing the dynamic damping law.

According to (20), the EL model is described as follows:

$$\begin{cases} \boldsymbol{v}_N^{\text{PBC}} = L_1 \frac{d\boldsymbol{i}_1^*}{dt} + \boldsymbol{v}_c + R_1 \boldsymbol{i}_1^* + r_{x1}(\boldsymbol{i}_1^* - \boldsymbol{i}_1) \\ -\boldsymbol{v}_{\text{PCC}} = L_2 \frac{d\boldsymbol{i}_2^*}{dt} - \boldsymbol{v}_c + R_2 \boldsymbol{i}_2^* + r_{x2}(\boldsymbol{i}_2^* - \boldsymbol{i}_2) \\ 0 = C_f \frac{d\boldsymbol{v}_c^*}{dt} - \boldsymbol{i}_1^* + \boldsymbol{i}_2^* + r_{x3}(\boldsymbol{v}_c^* - \boldsymbol{v}_c) \end{cases} \tag{32}$$

where $\boldsymbol{i}_1^*$, $\boldsymbol{i}_2^*$, and $\boldsymbol{v}_c^*$ are the references of $\boldsymbol{i}_1$, $\boldsymbol{i}_2$, and $\boldsymbol{v}_c$, respectively.

Substituting (2) and (3) into (32), (32) can be rewritten as follows:

$$\begin{cases} L_1 \left(\frac{d\boldsymbol{i}_1^*}{dt} - \frac{d\boldsymbol{i}_1}{dt} \right) + (R_1 + r_{x1})(\boldsymbol{i}_1^* - \boldsymbol{i}_1) = 0 \\ L_2 \left(\frac{d\boldsymbol{i}_2^*}{dt} - \frac{d\boldsymbol{i}_2}{dt} \right) + (R_2 + r_{x2})(\boldsymbol{i}_2^* - \boldsymbol{i}_2) = 0. \end{cases} \tag{33}$$

Defining the state variable error $\boldsymbol{e}_{i_1} = \boldsymbol{i}_1^* - \boldsymbol{i}_1$, $\boldsymbol{e}_{i2} = \boldsymbol{i}_2^* - \boldsymbol{i}_2$, (33) can be simplified to the following:

$$\begin{cases} L_1 \frac{d\boldsymbol{e}_{i_1}}{dt} + (R_1 + r_{x1})\boldsymbol{e}_{i_1} = 0 \\ L_2 \frac{d\boldsymbol{e}_{i_2}}{dt} + (R_2 + r_{x2})\boldsymbol{e}_{i_2} = 0. \end{cases} \tag{34}$$

Equation (34) is the first-order linear differential equation group. Under ideal continuous-time conditions, the general solution of (34) is expressed as follows:

$$\boldsymbol{e}_{i_1} = ce^{-\frac{R_1 + r_{x1}}{L_1} t}, \boldsymbol{e}_{i_2} = ce^{-\frac{R_2 + r_{x2}}{L_2} t}. \tag{35}$$

Equation (35) shows that once the parameters of *LCL*-filter are determined, the bigger the damping injected and faster the convergence of the state error to 0. However, existing research has revealed that excessive damping may increase the steady-state error of the system. In addition, the damping element r_{x1} affects the calculation of $\boldsymbol{v}_N^{\text{PBC}}$ in PBC, and $\boldsymbol{v}_N^{\text{PBC}}$ will be sent to PSMPC as the modified reference, excessive damping may affect the optimization of other objectives in PSMPC at the same layer as $\boldsymbol{v}_N^{\text{PBC}}$. Consequently, in this study, we propose an adaptive damping injection scheme as seen in Section V.

IV. Analysis of Existing MPC for LCL-3LT^{2}C

For MPC-controlled *LCL*-GCCs, it is important to solve the resonance problem. Additional control objectives associated with the filter are optimized to ensure the system stability. Owing to the coupling characteristics of the *LCL*-filter, the quality of grid current i_2 is affected by the converter current i_1 and filter capacitance voltages v_c, i_1, and v_c. They are usually selected as the control objectives for resonance suppression. To balance the NP voltage simultaneously, two existing MPC methods for *LCL*-3LT^{2}C are elaborated.

A. $\boldsymbol{i_1 i_2 \Delta v_{np}}$-MPC

It has been shown in [21] that with proper *LCL*-filter parameters, resonance can be mitigated when considering the optimization of $\boldsymbol{i}_1$. To achieve high-quality control of grid current and NP voltage balance in *LCL*-3LT^{2}C, the cost function of $i_1 i_2 \Delta v_{np}$ method is as follows:

$$\begin{aligned} J_{i_1 i_2 \Delta v_{np}} = & \left\| \boldsymbol{i}_2^*(k+1) - \boldsymbol{i}_2(k+1) \right\|_2^2 \\ & + \lambda_1 \left\| \boldsymbol{i}_1^*(k+1) - \boldsymbol{i}_1(k+1) \right\|_2^2 \\ & + \lambda_2 \left| \frac{T_s}{C_{\text{dc}}} |\boldsymbol{u}(k)|^T \boldsymbol{i}_1(k) + \Delta v_{np}(k) \right| \end{aligned} \tag{36}$$

where λ_1 and λ_2 are the weighting factors for resonance mitigation and NP voltage balance, respectively.

$i_1 i_2 \Delta v_{np}$ on its part suppresses the harmonics of $\boldsymbol{i}_1$ and $\boldsymbol{i}_2$ to ensure that the output current is not affected before and after passing the *LCL*-filter. However, the high-order harmonics of the filter capacitor voltage will lead to resonance energy oscillation, which is not considered in $i_1 i_2 \Delta v_{np}$, thereby limiting its resonance suppression capabilities. In addition, $i_1 i_2 \Delta v_{np}$ method has a poor robustness. Thus, once there is disturbance, the grid current will considerably be distorted.

B. $\boldsymbol{i_1 v_c i_2 \Delta v_{np}}$-MPC

Since the high-order harmonic components of $\boldsymbol{i}_1$, $\boldsymbol{v}_c$, and $\boldsymbol{i}_2$ can be regarded as the excitation source of resonance, reference [19] considered the predictive control of these three state variables. In *LCL*-3LT^{2}C, the cost function of $i_1 v_c i_2 \Delta v_{\text{dc}}$-MPC is expressed as follows:

$$\begin{aligned} J_{i_1 v_c i_2 \Delta v_{np}} = & \left\| \boldsymbol{i}_2^*(k+1) - \boldsymbol{i}_2(k+1) \right\|_2^2 \\ & + \lambda_1 \left\| \boldsymbol{i}_1^*(k+1) - \boldsymbol{i}_1(k+1) \right\|_2^2 \\ & + \lambda_2 \left| \frac{T_s}{C_{\text{dc}}} |\boldsymbol{u}(k)|^T \boldsymbol{i}_1(k) + \Delta v_{np}(k) \right| \\ & + \lambda_3 \left\| \boldsymbol{v}_c^*(k+1) - \boldsymbol{v}_c(k+1) \right\|_2^2 \end{aligned} \tag{37}$$

$$r_{x2\alpha\beta} = \frac{1}{(\boldsymbol{i}_{2\alpha\beta}^*(k) - \boldsymbol{i}_{2\alpha\beta}(k))} \left[-L_2 \frac{\boldsymbol{i}_{2\alpha\beta}^*(k+1) - \boldsymbol{i}_{2\alpha\beta}^*(k)}{T_s} + \boldsymbol{v}_{c\alpha\beta}^*(k) - R_2 \boldsymbol{i}_{2\alpha\beta}^*(k) - v_{PCC\alpha\beta}(k) \right], \text{if } : \boldsymbol{i}_{2\alpha\beta}^*(k) \neq \boldsymbol{i}_{2\alpha\beta}(k). \tag{29}$$

$$r_{x3\alpha\beta} = \left[\boldsymbol{v}_{c\alpha\beta}^*(k) - \boldsymbol{v}_{c\alpha\beta}(k) \right] \left[-C_f \frac{\boldsymbol{v}_{c\alpha\beta}^*(k+1) - \boldsymbol{v}_{c\alpha\beta}^*(k)}{T_s} + \boldsymbol{i}_{1\alpha\beta}^*(k) - \boldsymbol{i}_{2\alpha\beta}^*(k) \right], \text{if } : \boldsymbol{v}_{c\alpha\beta}^*(k) \neq \boldsymbol{v}_{c\alpha\beta}(k) \tag{31}$$

TABLE II
COMPARISON BETWEEN $i_1 i_2 \Delta v_{np}$, $i_1 v_c i_2 \Delta v_{np}$, AND DDPB-PSMPC

	(1) $i_1 i_2 \Delta v_{np}$	(2) $i_1 v_c i_2 \Delta v_{np}$	(3) DDPB-PSMPC ($\Delta v_{np} i_2 v_N^{con}$)
Objective numbers	3	4	3
Weighting factors	2	3	1
Resonance suppression	Limited, rely on proper LCL filter design	Effectiveness	Effectiveness
Robustness	Inferior	Better than (1)	Better than (2)

where λ_3 is the weighting factor of the filter capacitance. $i_1 v_c i_2 \Delta v_{np}$-MPC introduces more objectives for improving resonance suppression ability. However, its robustness is preferable to $i_1 i_2 \Delta v_{np}$-MPC.

C. Analysis and Comparison

To analyze the merits and demerits of both methods, the comparisons between $i_1 i_2 \Delta v_{np}$ and $i_1 v_c i_2 \Delta v_{np}$ are summarized in Table II. $i_1 i_2 \Delta v_{np}$ is very simple and can mitigate the resonance if proper *LCL*-filter parameters are set. However, when the filter parameter deviates from its nominal value, the resonance-suppression performance will become worse. Moreover, the robustness under $i_1 i_2 \Delta v_{np}$ is poor, meaning that the system stability may not be guaranteed if internal and external disturbances occur. The $i_1 v_c i_2 \Delta v_{np}$ method comprehensively considers state variables without affecting the power quality of the grid current. Hence, the resonance suppression ability and robustness are excellent. However, the number of control objectives increases, which offers a heavy computation burden and makes the selection of the weighting factor becoming more time-consuming. Additionally, when external disturbances occur, the anti-disturbance ability of $i_1 v_c i_2 \Delta v_{np}$ gets limited.

To effectively enhance the system anti-disturbance capability while minimizing the number of weighting factors, based on PBC with dynamic damping, a novel robust control called DDPB-PSMPC which has only three control objectiveness (e.g., $\Delta v_{np} i_2 v_N^{\text{con}}$) is proposed in this study. The characteristics of DDPB-PSMPC are also listed in Table II. Different with $i_1 i_2 \Delta v_{np}$ and $i_1 v_c i_2 \Delta v_{np}$ methods. DDPB-PSMPC improves the quality of the grid current and robustness while reducing weighting factors and control objectives.

V. PASSIVITY SMPC WITH DYNAMIC DAMPING INJECTION

To solve the problem of MPC being sensitive to disturbances and considering resonance suppression, PBC is considered in MPC to enhance the system robustness. To begin with, this section presents the integrated cost function of the proposed method. Furthermore, to obtain the output voltage of the PBC as modified reference in MPC, a detailed law for dynamic damping is designed. Finally, a PSMPC that assembles nonconflicting objectives in the same layer is introduced to reduce the weighting factor.

A. Integrated Cost Function of DDPB-PSMPC

MPC is advantageous in dealing with MOOP. Hence, it is convenient to embed the PBC into MPC. In this study, the converter voltage v_N is selected as the optimization objective of the MPC and the PBC output voltage v_N^{PBC} regarded as its reference. The disturbance is dampened by tracking the trajectory of v_N^{PBC}. Assuming $v_N^{\text{PBC}}(k) = v_N^{\text{PBC}}(k+1)$, the cost function of the proposed DDPB-PSMPC is expressed as follows:

$$\begin{aligned} J_{v_N i_2 \Delta v_n} = & \left\| i_2^*(k+1) - i_2(k+1) \right\|_2^2 \\ & + \lambda_2 \left| \frac{T_s}{C_{\text{dc}}} |u(k)|^T i_1(k) + \Delta v_{np}(k) \right| \\ & + \lambda_4 \left\| v_N^{\text{PBC}}(k+1) - v_N^{\text{con}}(k+1) \right\|_2^2 \end{aligned} \tag{38}$$

where λ_4 is the weighting factor of v_N. In (38), v_N^{PBC} replace i_1 to be tracked in the cost function, because v_N^{PBC} has included the optimization of $\boldsymbol{e}_{i_1}(\boldsymbol{i}_1^* - \boldsymbol{i}_1)$, so the term $(\boldsymbol{i}_1^*(k+1) - \boldsymbol{i}_1(k+1))$ has been removed from (38). Since the converter-side current $\boldsymbol{i}_1$ is indirectly controlled, the designed cost function (38) can also mitigate the resonance of *LCL*-filter.

Unlike existing MPC, DDPB-MPC considers energy dissipation and controls v_N^{con} instead of i_1 and v_c to improve performance. However, when calculating v_N^{PBC}, the damping term $\boldsymbol{R}_x$ in the EL model could affect both the stability and steady error. In the next section, following the influence of $\boldsymbol{R}_x$ on state variables, the dynamic damping rule is designed to obtain v_N^{PBC}.

B. Dynamic Damping Injection Law in PBC

According to the analysis in Section III, the damping matrix has conflicting effects on the convergence time and steady-state error. Thus, a new dynamic damping law is designed. The proposed method calculates the converter voltage v_N^{PBC} from the PBC as a reference for MPC. In (26), only the damping term r_{x1}^b has an impact on v_N^{PBC}, while damping network $\boldsymbol{R}_x$ is briefly rewritten as follows:

$$\boldsymbol{R}_x = \text{diag}\left[r_{x1}, r_{x1}, 0, 0, 0, 0\right]. \tag{39}$$

Since v_N^{con} couples with i_1, the converter-side current error e_{i_1} distorted v_N^{con}, and the proposed method uses the predicted error of i_1 to adjust the damping. First, the basic value of r_{x1}^b is determined experimentally and $\boldsymbol{R}_x^b$ is obtained ($\boldsymbol{R}_x^b = \text{diag}[r_{x1}^b, r_{x1}^b, 00, 00]$). With $\boldsymbol{R}_x^b$, the grid current maintains high quality without disturbance. Second, In DDPB-PSMPC, the error of converter-side current $\boldsymbol{e}_{i_1}$ need to be extrapolated. In the *n*-order Lagrange-Extrapolation [41] the error $\boldsymbol{e}_{i_1}(k+1)$ in the next period can be expressed as follows:

$$\boldsymbol{e}_{i_1}(k+1) = \sum_{l=0}^{n} (-1)^{n-l} \frac{(n+1)!}{l!(n+1-l)!} \boldsymbol{e}_{i_1}(k+l-n). \tag{40}$$

In general, the estimation error is large when $n = 1$ is applied. Hence, $n = 2$ is applied and the average error $e_{i_{1\_\text{avg}}}(k+1)$ is

obtained as follows:

$$\begin{cases} e_{i_{1\alpha}}(k+1) = 3e_{i_{1\alpha}}(k) - 3e_{i_{1\alpha}}(k-1) + e_{i_{1\alpha}}(k-2) \\ e_{i_{1\beta}}(k+1) = 3e_{i_{1\beta}}(k) - 3e_{i_{1\beta}}(k-1) + e_{i_{1\beta}}(k-2) \\ e_{i_{1\_\text{sum}}}(k+1) = e_{i_{1\alpha}}(k+1) + e_{i_{1\beta}}(k+1) \\ e_{i_{1\alpha\_\text{avg}}}(k+1) = e_{i_{1\_\text{sum}}}(k+1)/2. \end{cases} \tag{41}$$

Finally, if the average prediction error exceeds the threshold, dynamic damping $\boldsymbol{R}_x^a$ is added to $\boldsymbol{R}_x$ to overcome the disturbances. The integrated damping $\boldsymbol{R}_x$ is expressed as follows:

$$\boldsymbol{R}_x = \begin{cases} \boldsymbol{R}_x^b, \text{when} e_{i_{1\_\text{avg}}}(k+1) \le 5 \\ \boldsymbol{R}_x^b + \boldsymbol{R}_x^a, \text{when} e_{i_{1\_\text{avg}}}(k+1) > 5 \end{cases} \tag{42}$$

where $\boldsymbol{R}_x^a$ is calculated by the following:

$$\boldsymbol{R}_x^a = \text{diag}\left[e_{i_{1\_\text{sum}}}(k+1), e_{i_{1\_\text{sum}}}(k+1), 0, 0, 0, 0\right]. \tag{43}$$

The output voltage $\boldsymbol{v}_N^{\text{PBC}}$ of PBC is coupled with the converter-side current errors and injected damping. Considering the influence of above two variables on $\boldsymbol{v}_N^{\text{PBC}}$, the elements of the dynamic damping matrix $\boldsymbol{R}_x^a$ are quantified by errors of $\boldsymbol{i}_1$. According to (42), if $e_{i_{1\_\text{avg}}}(k+1) \le 5$ (here "5" is a tested value, which is used to evaluate whether the prediction error has been kept within the requirements), indicating that the average prediction error is small, the basic damping is enough to help *LCL*-3LT^{2}C maintain good performance. When $e_{i_{1\_\text{avg}}}(k+1) > 5$, $\boldsymbol{R}_x^a$ is required to dampen the disturbance. It should be noted that damping affects both the convergence time and steady error. When $e_{i_{1\_\text{avg}}}(k+1)$ exceeds the threshold, damping will be increases dynamically to ensure that the system converges quickly. Subsequently, the steady-state error is considered.

After the injection damping is determined, the converter-side voltage v_N^{PBC} based on the EL model is obtained as follows:

$$\boldsymbol{v}_{N\alpha\beta}^{\text{PBC}} = \boldsymbol{C}_{\text{PBC}}\boldsymbol{i} \tag{44}$$

where $\boldsymbol{C}_{\text{PBC}} = [\boldsymbol{I}_{2\times2}, \boldsymbol{O}_{2\times2}, \boldsymbol{O}_{2\times2}]$, and the input vector $\boldsymbol{i}$ is defined as $\boldsymbol{i} = [v_{N\alpha}^{\text{PBC}}, v_{N\beta}^{\text{PBC}}, -\boldsymbol{v}_{PCC\alpha}, -\boldsymbol{v}_{PCC\beta}, 00]^T$, and is calculated by (20).

The calculation steps for the output voltage in the PBC using the dynamic damping law are summarized in Algorithm I.

Algorithm I: PBC-Based on Active Damping Rejection.

Input: state variables and reference
Output: $\boldsymbol{v}_N^{PBC}$
Predict: $\boldsymbol{e}_{i_{1\alpha\beta}}(k+1)$
for $i = 1; i < 2; i++$
delay $\boldsymbol{e}_{i_{1\alpha\beta}}(k)$
$\boldsymbol{e}_{i_{1\alpha\beta}}(k-i) = \boldsymbol{e}_{i_{1\alpha\beta}}(k)$
end for
calculate: $\boldsymbol{e}_{i_{1\alpha\beta}}(k+1), \boldsymbol{e}_{i_{1\_avg}}(k+1) \rightarrow$ (41)
Active damping rejection: $\boldsymbol{R}_x \rightarrow$ (42)
If $\boldsymbol{e}_{i_{1\_avg}}(k+1) \le 5$
$\boldsymbol{R}_x = \boldsymbol{R}_b + \boldsymbol{R}_a$
else $\boldsymbol{R}_x = \boldsymbol{R}_b$
end if
EL model stablishes $\rightarrow$ (20)
calculate: $\boldsymbol{v}_N^{PBC} \rightarrow$ (44)

TABLE III
CANDIDATE SWITCHING WITH ABSOLUTE VALUE IN LAYER 1

Switching sequence	$\lvert u\rvert$	Description
1	0-0-0	Free candidates
2	1-1-1	
3	0-0-1	Limited candidates
4	0-1-0	
5	0-1-1	
6	1-0-0	
7	1-0-1	
8	1-1-0	

C. Design of PSMPC Controller

For the DDPB-MPC, there are two weighting factors in the cost function (38). The objective variables in (38) have different magnitudes, which means that it is time consuming to determine λ_2 and λ_4. To simplify the controller design, a new partial sequential model predictive control (PSMPC) is used to reduce the weighting factors. If there are s objectives in the MOOP, the general expression of the PSMPC can be written as follows:

$$\min f(x) = \min\left[f_1(x), f_2(x), \cdots, f_n(x)\right]^T \tag{45}$$

$$s.t. \begin{cases} x \in X, X \subseteq R_m \\ n < s \end{cases} \tag{46}$$

where $f_i(x)$ $(i = 12, \ldots, n)$ represents the division of MOOP into n-layer subproblems by PSMPC, subscript i is the optimization order and s is the number of control objectives. The constraint $(n < s)$ shows that the number of control layers in the PSMPC is less than the number of control objectives. This is because PSMPC optimizes nonconflicting control objectives in the same layer. This constraint $(n < s)$ ensures that the PSMPC overcomes the suboptimization problem caused by traditional SMPC.

In summary, different traditional SMPCs and proposed PSMPCs are not necessary to design an integrated cost function or layer for each objective. The proposed DDPB-PSMPC controls the nonconflicting targets in the same layers, thereby improving control performances and reduce the control objectives.

In *LCL*-3LT^{2}C, the control objectives are grid current i_2, converter voltage v_N^{con} and NP voltage Δv_{np}. DDPB-PSMPC inserts Δv_{np} into the first layer (Layer 1) for the following reasons: First, the prediction (13) of Δv_{np} has absolute value characteristics. Hence, the number of switching vectors are substantially reduced, thereby increasing the computational burden. In addition, the NP voltage balance impedes the unbalanced charges and discharges of the device, protecting the hardware setup.

When the NP voltage is arranged in the first layer of the SMPC, the switching vectors reduces from 27 to 8. The absolute switching vectors are listed in Table III.

Taking (13) as the cost function for Δv_{np} in layer 1 to balance the NP voltage, J_{layer1} can be expressed as follows:

$$J_{\text{layer1}}(|\boldsymbol{u}_k|) = \frac{T_s}{C_{\text{dc}}}|\boldsymbol{u}_k|^T i_1(k). \tag{47}$$

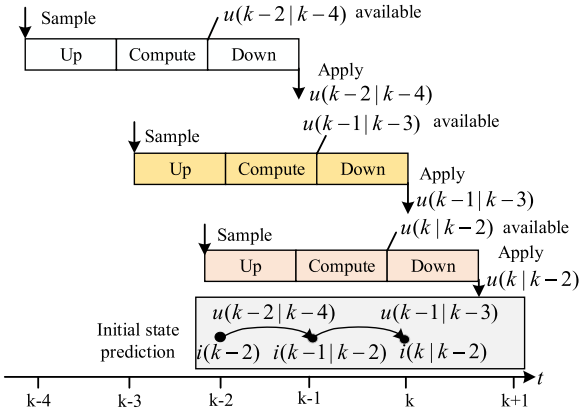

Fig. 3. Compensation of a time-delay of two sampling intervals, using an initial state prediction.

The implementations of Layer 1 and 2 in PSMPC are illustrated in Fig. 3 and explained as follows:

Layer 1: J_{layer1} represents the change in Δv_{np} in one sampling period. In Table III, the cost of free candidates equals 0. Consequently, the free candidates avoid the cost function calculation in (38), which further alleviates the computational burden. Contrarily, the cost of limited candidates varies. Based on this rule, the candidate-reservation law in layer 1 is as follows:

1) After removing the absolute value, the free candidates that comprise set $\boldsymbol{u}^f$ will be sent to the next layer directly without cost calculation.
2) The cost of the limited candidates is calculated and classified according to (47). If $J_{\text{layer1}}(|\boldsymbol{u}_k|) \geq 0$, after removing the absolute value, candidates belonging to $\boldsymbol{u}_k$ are added to the positive set $\boldsymbol{u}^+$. If $J_{\text{layer1}}(|u_k|) < 0$, $\boldsymbol{u}_k$ would belong to negative set $\boldsymbol{u}^-$.
3) Sampling and calculating the voltage difference signal $\Delta v_{np}(k)$, if $\Delta v_{np}(k) \geq 0$, the set $\boldsymbol{u}^f \cup \boldsymbol{u}^-$ is saved. Conversely, the set $\boldsymbol{u}^f \cup \boldsymbol{u}^+$ is applied to the next layer. (Note that the number of reserved candidates in Layer 1 is changeable, assuming N represents the reserved vectors).

Layer 2: In PSMPC, the optimization of v_N^{con} suppresses the resonance and improved the anti-disturbance ability of grid current i_2. Thus, v_N^{con} and i_2 are placed in the second layer (layer 2) for simultaneous optimization. Since both control objectives has different units and reference levels, a correction factor λ_c is assigned to v_N^{con}. The integrated cost function for i_2 and v_N^{con} is designed as follows:

$$J_{\text{layer2}} = \|i_2^*(k+1) - i_2(k+1)\|_2^2 + \lambda_c \left\|v_N^{\text{PBC}}(k+1) - v_N^{\text{con}}(k+1)\right\|_2^2 \quad (48)$$

where λ_c is the weighting factor for v_N^{con}, which should be properly selected to guarantee the tracking errors of $\boldsymbol{i}_2$ and $\boldsymbol{v}_N^{\text{con}}$ are in the same order of magnitude. Then it can also be used as a tradeoff between robustness and output current quality.

In (48), N candidates are inputted into layer 2, which simultaneously considered the anti-disturbance ability and quality of the grid current. The final optimal vector ensures the performance of the output current when disturbance occurred.

Algorithm II: DDPB-PSMPC Method.

Input: variables and references
Output: $\boldsymbol{u}_{opt}(k)$
Initialization: $\boldsymbol{U}^f$, $u^i(k) \in |\boldsymbol{U}_1| - \boldsymbol{U}^f$
for $(i = 1; i < 6; i++)$
$J^i_{layer1} = J_{layer1}(|\boldsymbol{u}^i(k)|)$
Revivification $|\boldsymbol{u}^i(k)| \rightarrow \boldsymbol{U}^i(k)$
if $J^i_{layer1} \geq 0$ $\boldsymbol{U}^i(k) \subseteq \boldsymbol{U}^+$
else $\boldsymbol{U}^i(k) \subseteq \boldsymbol{U}^-$
end if
end for
if $\Delta v_{dc} \geq 0$ $\boldsymbol{U}_2 = \boldsymbol{U}^+ \cup \boldsymbol{U}^f$
else $\boldsymbol{U}_2 = \boldsymbol{U}^- \cup \boldsymbol{U}^f$
end if
for $(i = 1, i < N, i++)$
$J^i_{layer2} = J_{layer2}(\boldsymbol{U}^i_2)$
end for
$u_{opt}(k) = \underset{u(k)}{argmin}\{J^i_{layer2}(u(k))|^{u(k) \in U_2}_{i = 1 \cdots N}\}$

D. Implementation of DDPB-PSMPC Controller

Fig. 4 shows the control block diagram of the DDPB-SMPC method, which includes the following modules: Clarke transform, Kalman filter, prediction model, PBC with dynamic damping injection, and new SMPC module. The algorithm for the DDPB-PSMPC is shown in Algorithm II.

It is needed to note that revivification here indicates removing the absolute symbol of (13) and restoring all the available candidate vectors. For instance, the switching sequence (11 0) has the same results in J_{layer1} calculation with the switching sequences (–1 –10), (–11 0), and (1 –10). After revivification, the candidate vectors from layer 1 to 2 for the switching sequence (11 0) will be restored to four candidate vectors [i.e., (–1 –10), (–11 0), (1 –10), and (11 0)].

In summary, the implementation of DDPB-PSMPC is explained as follows:

1) Grid current i_2 and grid voltage v_g are sampled at instance k. Then, to reduce the number of sampling sensors, the converter-side current i_1 and voltage of the filter capacitance v_c are estimated using the Kalman filter. Subsequently, the prediction model of *LCL*-3LT^{2}C is obtained using (7).
2) By calculating the tracking error $e_{i_1}(k)$using the Lagrange-extrapolation method, the prediction error $e_{i_1}(k+1)$ is obtained. Based on the damping injection law in (42), $\boldsymbol{R}_x$ is determined and the output voltage v_N^{PBC} based on the EL models (20) and (44) is calculated. v_N^{PBC} is sent to the SMPC as a modified reference of v_N.
3) According to NP voltage $\Delta v_{np}(k)$ in (13), the N candidates saved in layer 1 are all inputted into layer 2. Since the optimization of i_2 and v_N focuses on the quality of the

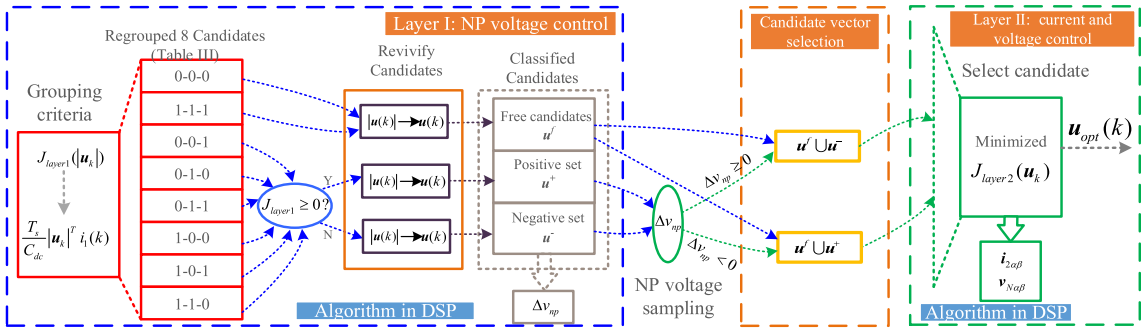

Fig. 4. Flowchart of the proposed two-layer PSMPC controller.

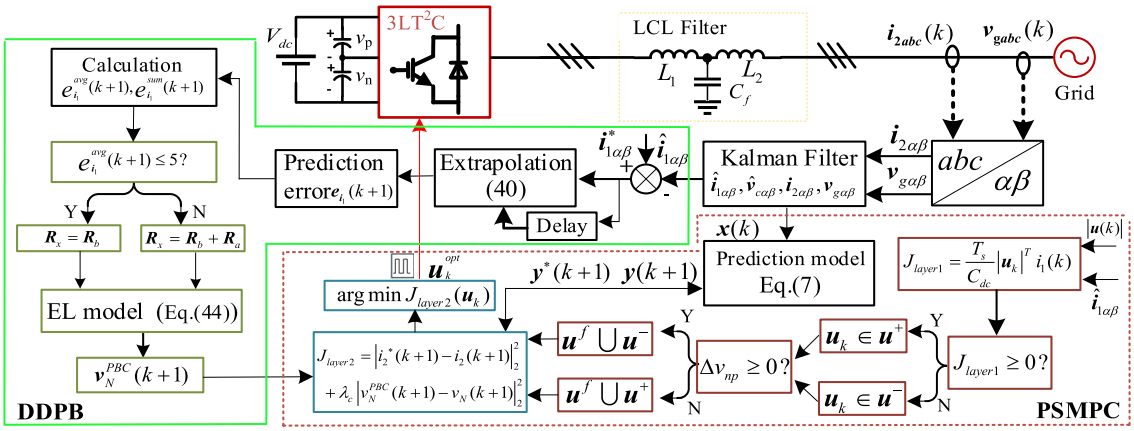

Fig. 5. Block diagram of the DDPB-PSMPC control for *LCL*-3LT^{2}C GCC.

grid current, both objectives are arranged in layer 2. By tracking v_N^{PBC}, the robustness of the *LCL*-3LT^{2}C GCCs is improved by PSMPC. Finally, the optimal vector with the minimum J_{layer2} is selected.

E. Time-Delay Analysis

So far, we have assumed an ideal discrete-time setup without any time delay between the sampling of the measurements and the application of the new switch position. In a practical setting of the T-type converter, however, physical limitations cause a time-delay between the sampling of the measurements and the application of the new switch position. The most prominent and commonly encountered sources of delays contain: measurement delay, uplink communication delay, computation delay, downlink communication delay, and actuation delay.

To compensate the time-delay in practice, as shown in Fig. 5, we add *Step* 0 to the control algorithm. *Step* 0 performs the initial state prediction and projects the stator current sample from time step *k*-1 to *k*. Also, the grid current reference needs to be projected one time-step forward. With the given grid current reference. At time step $k-1$, the predictive current control algorithm computes $\boldsymbol{u}_{\mathrm{opt}}\,(k|k\,-\,1)$, which is applied at time-step *k*. This procedure is repeated at the next time step.

1) The grid current at time step $k-1$ is sampled, and the current at time step k is predicted using the initial state prediction (7).
2) Given the switch position $\boldsymbol{u}\ (k-1|k-2)$ and considering the constraints on the switching transitions, the set of admissible switch positions at time step k, $\mathrm{U}(k|k-1)$, is determined.
3) For each switch position $u(k|k-1)\ \epsilon\ \mathrm{U}(k|k\ -\ 1)$, the grid current at time step k+1, is $(k+1)$, is predicted using the model (7).
4) The switch position $\boldsymbol{u}_{\mathrm{opt}}(k|k-1)$ with the minimum cost is determined and applied to the inverter.

F. Stability Analysis

Considering that the contribution of this article is to combine dynamic damping injection of PBC control with model predictive. Therefore, the stability analysis here aims to demonstrate the stability of *LCL*-interfaced grid-connected converter with MPC controller. Assume that the description of a state-space model considering the model uncertainty is

$$\begin{cases} \boldsymbol{x}\ (k+1) = \ \boldsymbol{A}\boldsymbol{x}\,(k) + \boldsymbol{B}\boldsymbol{u}\,(k) + \boldsymbol{T}\boldsymbol{d}\,(k) \\ \mathbf{y_c}\ (k) = \boldsymbol{\lambda_c}\,\boldsymbol{x}\,(k) \end{cases} \tag{49}$$

Where $\boldsymbol{x}(k) \in \mathbb{R}^{n_x}$ is the state variable, $\boldsymbol{u}(k) \in \mathbb{R}^{n_u}$ is the input control variable, $\boldsymbol{y_c}(k) \in \mathbb{R}^{n_c}$ is the output control variable, and $\boldsymbol{d}(k)$ is equal to $\boldsymbol{v_g}(k)$. Note that, here, the grid voltage is defined as the disturbance.

To reduce the steady-state error, we can rewrite the system of (49) as an increment model as follows:

$$\Delta \boldsymbol{x}\ (k+1) = \mathbf{A}\Delta \boldsymbol{x}\,(k) + \boldsymbol{B}\Delta \boldsymbol{u}\,(k) + \boldsymbol{T}\Delta \boldsymbol{d}\,(k) \tag{50}$$

where $\Delta x\ (k) = x(k) - x(k-1)$, $\Delta u\ (k) = u(k) - u(k-1)$, $\Delta d\ (k) = d(k) - d(k-1)$. The system prediction error at instant $k+1$ can be expressed as follows:

$$\begin{aligned} \boldsymbol{E}_P\ (k+1|k) &= \boldsymbol{R}\,(k+1) - \boldsymbol{Y}\,(k+1) \\ &= \boldsymbol{R}\,(k+1) - \boldsymbol{S}_x\ \Delta x\,(k) - \urcorner \mathbf{y_c}\,(k) \\ &\quad - \boldsymbol{S_d}\Delta d\,(k) - \boldsymbol{S_u}\Delta \boldsymbol{u}\,(k) \end{aligned} \tag{51}$$

where

$$\boldsymbol{S}_x = \left[\boldsymbol{\lambda A}\ \boldsymbol{\lambda A}^2\ \boldsymbol{\lambda A}^3 \ldots\ \boldsymbol{\lambda A}^N\right]^T$$

$$\urcorner = [\boldsymbol{I}_{nc\times nc}\ \boldsymbol{I}_{nc\times nc}\ \ldots\ \boldsymbol{I}_{nc\times nc}]^T$$

$$\boldsymbol{S_d} = \begin{bmatrix} \boldsymbol{\lambda B} & 0 & \cdots & 0 \\ \boldsymbol{\lambda AB} & \boldsymbol{\lambda B} & \cdots & 0 \\ \vdots & \vdots & \ddots & \vdots \\ \boldsymbol{\lambda A}^{N-1}\boldsymbol{B} & \boldsymbol{\lambda A}^{N-2}\boldsymbol{B} & \cdots & \boldsymbol{\lambda B} \end{bmatrix}$$

$$\boldsymbol{S_u} = \begin{bmatrix} \boldsymbol{\lambda T} & 0 & \cdots & 0 \\ \boldsymbol{\lambda AT} & \boldsymbol{\lambda T} & \cdots & 0 \\ \vdots & \vdots & \ddots & \vdots \\ \boldsymbol{\lambda A}^{N-1}\boldsymbol{T} & \boldsymbol{\lambda A}^{N-2}\boldsymbol{T} & \cdots & \boldsymbol{\lambda T} \end{bmatrix}.$$

Based on the principle of MPC, only the first element of the open-loop optimal control sequence acts on the T-type converter, i.e.

$$\Delta \boldsymbol{u}\ = \left[\boldsymbol{I}_{nc\times nc}\quad 0\quad \cdots\quad 0\ \right]\ \Delta \boldsymbol{U}^*\,(k) \tag{52}$$

where $\Delta \boldsymbol{U}^*$ is the optimal control sequence, expressed as follows:

$$\Delta \boldsymbol{U}^*\ (k) = \left(\boldsymbol{S}_u^T\boldsymbol{\Gamma}_y^T\boldsymbol{\Gamma}_y\boldsymbol{S}_u + \boldsymbol{\Gamma}_u^T\boldsymbol{\Gamma}_u\right)^{-1}\boldsymbol{S}_u^T\boldsymbol{\Gamma}_y^T\boldsymbol{E}_P\,(k+1|k)\,. \tag{53}$$

Defining the control gain $\boldsymbol{K}_{\text{mpc}}$ of the prediction controller as follows:

$$\begin{aligned} \boldsymbol{K}_{\text{mpc}} = &\left[\boldsymbol{I}_{nc\times nc}\quad 0\quad \cdots\quad 0\right]_{1\times m}\left(\boldsymbol{S}_u^T\boldsymbol{\Gamma}_y^T\boldsymbol{\Gamma}_y\boldsymbol{S}_u\right. \\ &\left. +\ \boldsymbol{\Gamma}_u^T\Gamma_u\right)^{-1}\boldsymbol{S}_u^T\boldsymbol{\Gamma}_y^T\boldsymbol{E}_P\,(k+1|k)\,. \end{aligned} \tag{54}$$

$\Delta \boldsymbol{u}(k)$ can be derived using (47) and (48) as follows:

$$\begin{aligned} \Delta \boldsymbol{u}\ (k) &= \boldsymbol{K}_{\text{mpc}}\ \boldsymbol{E}_P\,(k+1|k) \\ &= \boldsymbol{K}_{\text{mpc}}\ (\boldsymbol{R}\,(k+1) - \boldsymbol{S}_x\Delta \boldsymbol{x}\,(k) \\ &\quad - \urcorner\boldsymbol{\lambda_c}\boldsymbol{x}\,(k)\ - \boldsymbol{S_d}\Delta \boldsymbol{d}\,(k) \\ &= \boldsymbol{K}_{\text{mpc}}\ \boldsymbol{R}\,(k+1) - \boldsymbol{K}_{\text{mpc}}\,(\boldsymbol{S_x} + \urcorner\boldsymbol{\lambda_c})\,\Delta \boldsymbol{x}\,(k) \\ &\quad - \boldsymbol{K}_{\text{mpc}}\urcorner\boldsymbol{\lambda}_c x\,(k-1) - \boldsymbol{K}_{\text{mpc}}\ \boldsymbol{S}_d\Delta d\,(k)\,. \end{aligned} \tag{55}$$

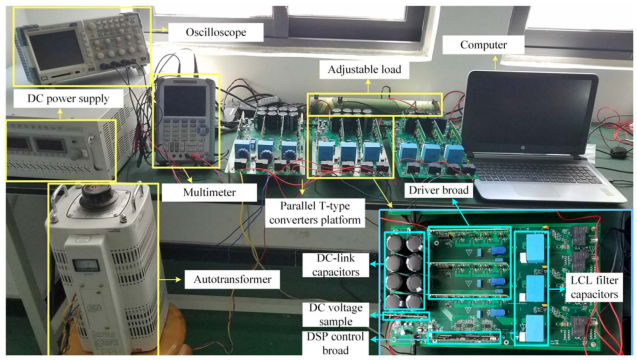

Fig. 6. Experiment platform and designed 3LT^{2}C.

Thus, the closed-loop system can be expressed as follows:

$$\begin{aligned} \Delta \boldsymbol{x}\ (k+1) = &\left(\boldsymbol{A} - \boldsymbol{BK_{\text{mpc}}}\,(\boldsymbol{S}_x + \urcorner\boldsymbol{\lambda}_c)\right)\ \Delta \boldsymbol{x}\,(k) \\ &+\ \boldsymbol{BK}_{\text{mpc}}\boldsymbol{R}\,(k+1) + (\boldsymbol{T} - \boldsymbol{BK}_{\text{mpc}}S_d) \\ &\Delta \boldsymbol{d}\,(k) - \boldsymbol{BK}_{\text{mpc}}\urcorner\boldsymbol{\lambda}_c\boldsymbol{x}\,(k-1)\,. \end{aligned} \tag{56}$$

Therefore, when all the characteristic roots of the matrix $\boldsymbol{A} - \boldsymbol{BK}_{\text{mpc}}(\boldsymbol{S_x} + \urcorner\boldsymbol{\lambda_c})$ are located within the unit circle, the closed-loop control system is stable. For an *LCL*-interfaced T-type grid-connected converter, $\boldsymbol{K}_{\text{mpc}}$ is the optimal switching sequence that can minimize the cost function, which should satisfy $|\boldsymbol{A} - \boldsymbol{BK}_{\text{mpc}}(\boldsymbol{S_x} + \urcorner\boldsymbol{\lambda_c})| < 1$. Thus, for the MPC control problem without constraints, the calculated $\boldsymbol{K}_{\text{mpc}}$ should be substituted to the characteristic roots of the matrix $\boldsymbol{A} - \boldsymbol{BK}_{\text{mpc}}(\boldsymbol{S_x} + \urcorner\boldsymbol{\lambda_c})$. The one that does not satisfy the characteristic equation should not be selected. Thus, the selected $\boldsymbol{K}_{\text{mpc}}$ among all the switching sequences can guarantee the system stability.

VI. Experimental Results

A. Hardware Setup

1) Experimental Platform: To verify the effectiveness of the proposed DDPB-PSMPC method, a three-phase *LCL*-3LT^{2}C GCC with a rated power of 10 kW at 380 V ac 50 Hz was built in the laboratory. The rated nominal and max input voltage at 500 V and 1000 V dc, the converter efficiency may reach a semiconductor efficiency of 8 kHz. These features reduce the size of magnetics for the *LCL*-filter design and as a result a higher power density.

The laboratory platform is shown in Fig. 6. In the experiment, A programmable ac source Chroma 6590 is applied to emulate the harmonics and impedance of the grid. The DDPB-PSMPC algorithm is executed using a 32-bit floating-point digital signal processor (DSP-TMS320F28379 from Texas Instruments Company), which is typically used for fast and complex digital calculations and control algorithm implementations. The 3LT^{2}C converter (see Fig. 1) comprised six 1MBH50D-060 (600 V/50 A) insulated gate bipolar transistors (IGBTs) and six 2MBI150U2A-060 (600 V/150 A) IGBTs for vertical and horizontal bridges, respectively. The hardware platform parameters are listed in Table IV. In addition, to purpose a fair competition,

TABLE IV
FILTER DESIGN SPECIFICATIONS

Parameters	Symbol	Value
Average switching frequency	f_{SW}	22 kHz
Ripple coefficient	$\%ripple$	2.5%
reactive power of filter capacitor	$\%x$	5%
Ratio	r	0.5

TABLE V
PARAMETER SPECIFICATION

PARAMETERS	SYMBOL	VALUE
RATED POWER	P_e	$10\,KW$
DC-LINK VOLTAGE	V_{dc}	$500\,V$
GRID VOLTAGE (RMS)	e_g	$110\,V$
GRID FREQUENCY	f_g	$50\,Hz$
DC-LINK CAPACITANCE	C_{dc}	$560\,\mu F$
CONVERTER- AND GRID-SIDE INDUCTANCE	L_1, L_2	$4\,mH, 2\,mH$
FILTER CAPACITANCE	C_f	$4\,\mu F$
CONVERTER-SIDE RESISTANCE	R_1	$0.26\,\Omega$
GRID-SIDE RESISTANCE	R_2	$0.26\,\Omega$
SAMPLING TIME	T_s	$20\,\mu s$
WEIGHTING FACTOR	λ_c	1/8

TABLE VI
PARAMETER SPECIFICATION OF MPC CONTROLLER

Method	Symbol	Explanation	Value
A-MPC ($i_1 i_2 \Delta v_{np}$)	λ_1	Weighting factor of i_1	0.90
	λ_2	Weighting factor of Δv_{np}	3
B-MPC ($i_1 v_c i_2 \Delta v_{np}$)	λ_1	Weighting factor of i_1	0.95
	λ_2	Weighting factor of Δv_{np}	2.5
	λ_3	Weighting factor of v_c	0.05
DDPB-PSMPC	λ_c	Weighting factor of v_N^{con}	0.125

the detailed parameters of proposed DDPB-PSMPC and traditional MPC (including A-MPC and B-MPC) methods are shown in Table VI.

In experiment, to verify the effectiveness of the proposed controller under weak and unbalanced grid, a grid emulator Chroma 61800 is used, which can be applied to the test of general electrical products (e.g., household appliances, switching power supply).

2) Computation Burden Analysis and Requirement for the Microprocessor: To implement and compare the three typical predictive controllers, namely, DDPB-PSMPC, A-MPC, and B-MPC methods, the calculation burden analysis is required. To evaluate the computation burden of different control methods, two breakpoints are set in the program debugging environment CCS10.1 for the digital-signal-processor (TMS320F28379D), the time difference between the two breaking points is the calculation time. The results indicate that, the calculation time for DDPB-PSMPC takes about 44 μs, compared with 42 and 45 μs with A-MPC and B-MPC methods. indicating that DDPB-PSMPC method consumes similar computation burthen as two traditional MPC methods. For DDPB-PSMPC, it is necessary to calculate the passive converter side voltage v_N^{PBC} as the reference of v_N^{con} and determine the damping term $\boldsymbol{R}_x$ before applying PSMPC, the computation burthen is increased. However, when calculating the cost function of layer I in PSMPC, the absolute value characteristics of the NP voltage cost function (47) are used, the switching vectors are reduced from 27 to 8, so the number of cost function calculations is reduced. However, as for two traditional methods, 27 switching vectors are required for (36) and (37).

3) Selection of LCL-Filter Parameters: The typical formulas for calculation of the *LCL*-filter parameters are given as follows [42], [43]:

1) *Selection of* L_1

The primary component is the inverter inductance, or L_1, which can be derived using

$$L_1 = \frac{V_{dc}}{8 \times f_{\text{SW}} \times i_{ge} \times \%\text{ripple}} \tag{57}$$

Where f_{SW}, V_{dc}, i_{ge} and $\%$ripple represent the switching frequency, dc-link voltage, rated grid current, and percentage of the current variations.

2) *Selection of* C_f

The sizing of the primary filter capacitor C_f is handled in a similar fashion using (58)

$$C_f \le \frac{\%x \times Q_{\text{rated}}}{2\pi f_g \times \text{V}_g^2} \tag{58}$$

Where $\%x$, Q_{rated}, f_g, and V_g are the percentage of the total reactive power absorbed by the filter capacitor, the rated reactive power, the grid frequency, and grid voltage.

3) *Selection of* L_2

For L_2 design, the attenuation factor I_{att} can be derived as follows:

$$I_{\text{att}} = \frac{1}{\left|1 + r \times \left(1 - L_1 \cdot C_b \cdot (2\pi f_{\text{sw}})^2 x\right)\right|} \times 100\% \tag{59}$$

Where r is the ratio between the two inductors, which can be derived as $r = \left|\frac{I_{\text{att}}-1}{1-L_1 \times C_f \times (2\pi f)^2}\right|$. Thus, the resultant value for L_2 is then given as $L_2 = r \times L_1$.

Based on (57)–(59), the design parameter requirements are selected in Table IV and the resulted *LCL*-filter parameters as well as the weighting factors are given in Tables V and VI.

B. Grid Current Without Disturbance

Compared to $i_1 i_2 v_{np}$-MPC (referred as "A-MPC") and $i_1 v_c i_2 v_{np}$-MPC (referred as "B-MPC"), the merits of proposed DDPB-PSMPC are evaluated under the following three scenarios.

1) Steady-state responses of grid current and harmonic distribution analysis.
2) Dynamic responses of the grid current when reference current increases from 15 to 30 A.
3) Balance ability of the NP voltage.

1) Steady-State Response: Fig. 7 shows the steady-state waveform and harmonic distribution analysis of grid currents

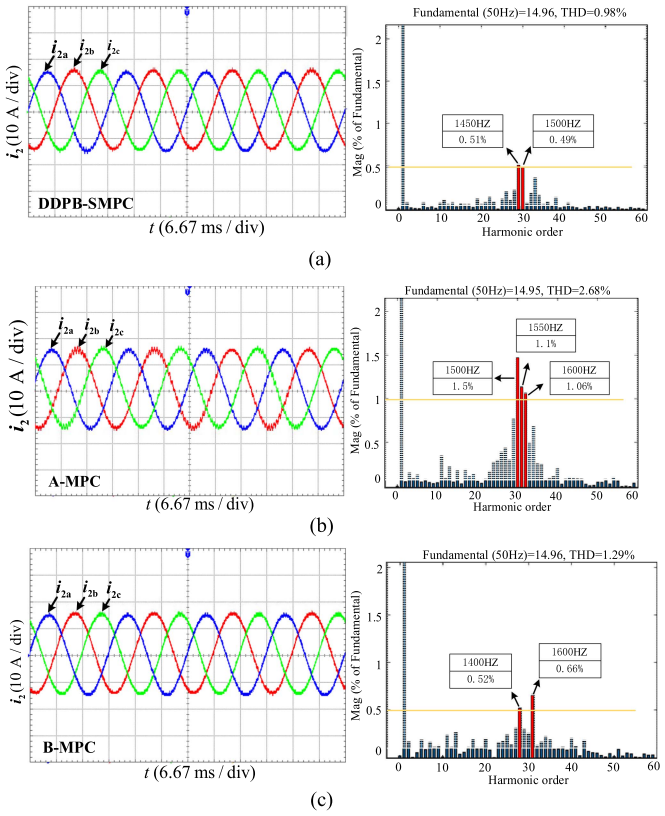

Fig. 7. Steady-state grid current and harmonic distribution. (a) DDPB-PSMPC. (b) A-MPC. (c) B-MPC.

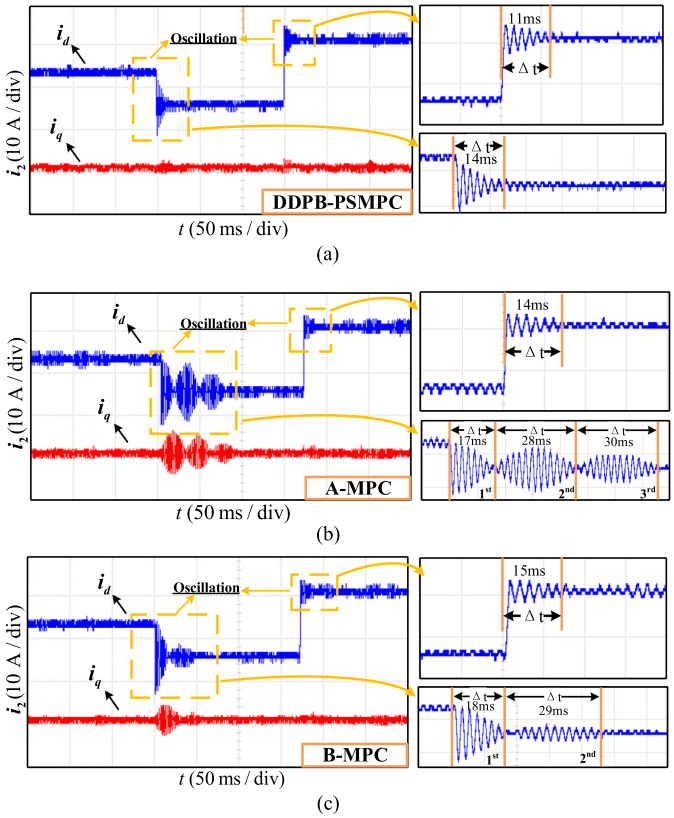

Fig. 8. Dynamic response of the grid current under *dq*-frame. (a) DDPB-PSMPC. (b) A-MPC. (c) B-MPC.

with a reference of 15 A. The THD of DDPB-PSMPC, A-MPC, and B-MPC were 0.98%, 2.68%, and 1.29%, respectively. With DDPB-PSMPC, the maximum harmonic distribution of grid was 0.51%, whereas those of A-MPC and B-MPC are 1.5% and 0.66%, respectively. This shows that the DDPB-PSMPC has the best harmonic suppression capability. Furthermore, the DDPB-PSMPC maintains a very low harmonic content in the low-frequency range.

2) Dynamic Response: To further compare the dynamic response of the three methods, dynamic response experiment is carried out under unbalanced grid. Fig. 8(a) shows that the proposed method has the fastest dynamic response time. The grid current is transformed to the *dq*-frame and the unbalance degree of the grid voltage is 30% (the unbalanced grid condition is realized by Chroma 61800). A step-down of the reference current first occurs from 15 to 5 A, and then rises to 20 A after 0.15 s. When the reference current drops, with DDPB-PSMPC, i_d is stabilized after about 14 ms. Then, when the reference rises from 5 to 20 A, i_d stably tracks its reference after 11 ms. Also, as shown in Fig. 8(a), because of the injected damping, the changes of its reference have slight effect on i_q , the coupling between i_d and i_q can be ignored.

For the A-MPC method in Fig. 8(b), when the reference decreases, both i_d and i_q undergo obvious transient oscillations. Take i_d as an example, it restores stable state after three oscillations (about 75 ms in total). When the reference rises, it is stabilized after about 14 ms. With B-MPC method in Fig. 8(c), i_d and i_q oscillate twice (about 47 ms in total) when the reference is decreased, and the performance is similar with that of the A-MPC controller when the current is increased.

In summary, compared to A-MPC and B-MPC methods, DDPB-PSMPC reduces one optimization objective and has less fluctuations as well as fastest dynamic response, which further proves its superiority.

3) Balance of the Neutral-Point (NP) Voltage: For a 3LT^{2}C converter, it is vital to balance the NP voltage. Fig. 9(a)–(c) show the NP voltage difference Δv_{np} when the reference current is 15 A. It can be clearly observed that Δv_{np} is efficiently suppressed with DDPB-PSMPC, A-MPC, and B-MPC methods. The fluctuation range of Δv_{np} is limited to [–100 mV, +200 mV].

C. Robustness Analysis

To verify the robustness of the proposed method, two scenarios are tested.

1) The anti-disturbance capability under parameter variations of the *LCL*-filter.
2) Grid current nonlinear filter parameters.
3) Robust performance of the grid current and voltage under external disturbances (e.g., grid inductance changes, distorted

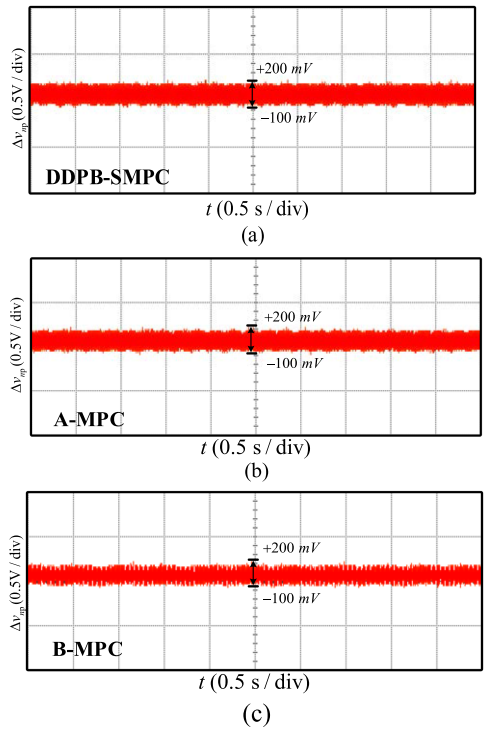

Fig. 9. Neutral-point voltage variations ΔV_{np}. (a) DDPB-PSMPC. (b) A-MPC. (c) B-MPC.

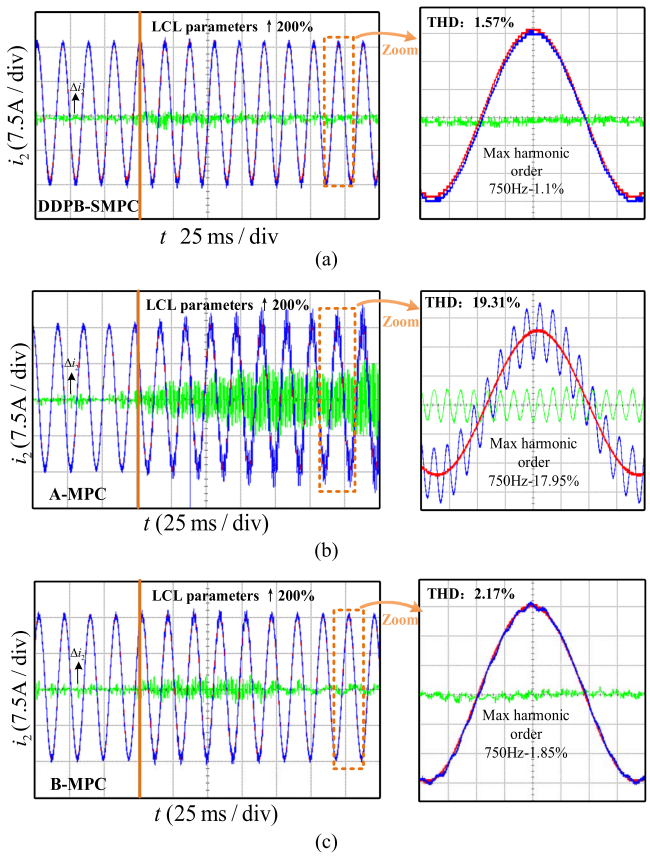

Fig. 10. Grid current under an increase of the *LCL*-filter parameters. (a) DDPB-PSMPC. (b) A-MPC. (c) B-MPC.

grid voltage, and low-voltage ride through testing (LVRT) capability.

4) Tracking performance of the grid current under unbalanced grid.

1) Grid Current Under Filter Parameter Variations: For 3LT^{2}C GCCs, the internal disturbance mainly originates from the changes in the *LCL*-filter parameters. This experiment aims to verify the robustness and output performance of the system under parameter mismatches.

Fig. 10 shows the waveforms of the grid current with the DDPB-PSMPC, A-MPC, and B-MPC methods. The parameters of *LCL*-filter in Table II increased by 200%. The results show that the A-MPC method could not track the reference consistently, revealing that it is sensitive to parameter changes. When internal disturbance occurs, the THD of grid current with DDPB-PSMPC is 1.57%, which is 28% lower than that with B-MPC. The content of the maximum harmonic order (750 Hz) is 1.1%, while that with B-MPC is 1.85%.

Fig. 11 shows the grid current when parameters of *LCL*-filter decreased by 50%. The grid current under A-MPC components contained rich harmonic, indicating that the performance of A-MPC is the worst. For DDPB-PSMPC, the THD and maximum harmonic distribution of grid current are 3.40% and 1.1%, respectively, which are slightly higher than B-MPC.

2) Grid Current Under Nonlinear Filter Parameters: To verify the performing of the proposed PPPB-PSMPC under more complex load condition with nonlinear characteristics. The grid-side inductance L_2 is replaced by a nonlinear inductance with magnetic flux saturation characteristics of the iron core, where the nonlinear characteristics of the magnetic flux and the current are approximately expressed as follows [44], [45]:

$$\phi = \frac{1}{1000}\tanh\left(\frac{I}{10}\right) \tag{60}$$

Where ϕ is the flux of iron core in nonlinear inductance, and I represents the inductor current. Equation (60) shows that the inductance is changeable with its current. It is needed to note that, (54) is an experienced expression, the magnetic flux is influenced by many factors, thus (60) may not be so accurate in practice.

In experiment, to achieve fast switching between different grid-side inductance and ensure that its current will not interrupt, the designed filter switching circuit is shown in Fig. 12. S_1 and S_2 are bidirectional power transistors. In normal operation, $S_2$is turned OFF and S_1 is turned ON. After several microseconds, S_2 is turned ON and S_1 is turned OFF, the nonlinear inductance L_{2x} is series connected with L_1 and C_f.

Fig. 13 shows the waveforms of the grid current with nonlinear inductance under three methods. Fig. 13(a) depicts the nonlinear relationship of magnetic flux versus current in (60). When the inductance current changes continuously, the magnetic flux does not change linearly. Therefore, when the output current passes through the inductance, its value exhibits nonlinear variation.

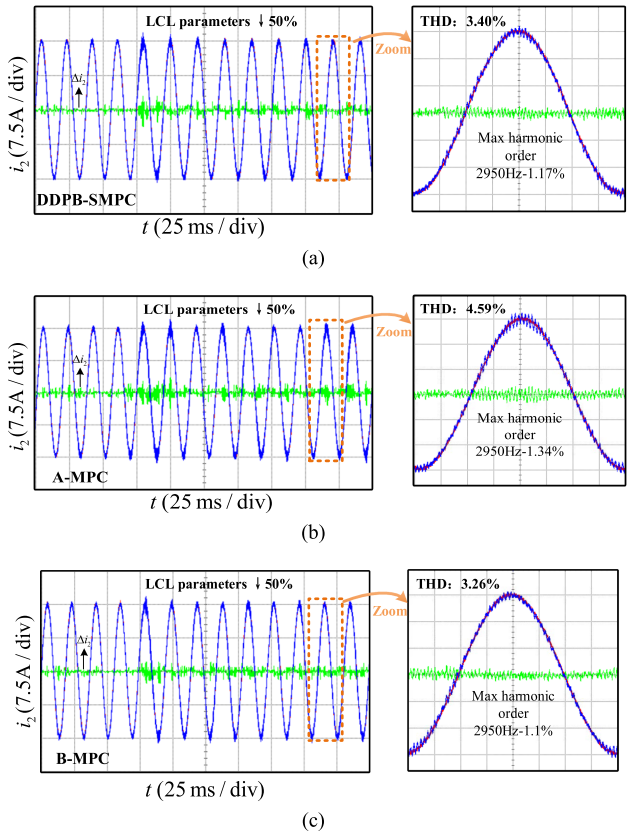

Fig. 11. Grid current under a decrease of *LCL*-filter parameters. (a) DDPB-PSMPC. (b) A-MPC. (c) B-MPC.

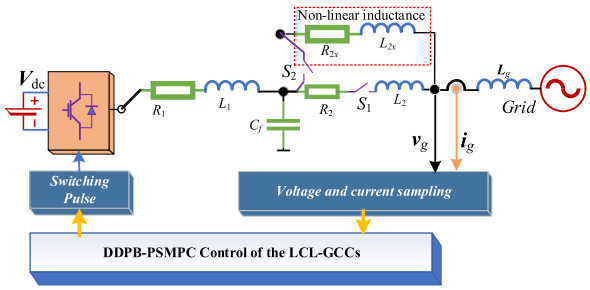

Fig. 12. Block diagram of the experimental *LCL*-GCCs with different groups of filter parameters.

When switching to the nonlinear inductance, among the three methods, the distortion of grid current under DDPB-PSMPC is the slightest, and its THD is the lowest (8.8%). Compared with DDPB-PSMPC, the THD of A-MPC increased by 3.8%, and grid current is distorted seriously. The THD of B-MPC method (10.7%) was lower than that of AMPC (12.6%), but higher than that of DDPB-PSMPC.

3) Grid Current Under External Disturbances:

a) Impact of grid impedance: For external disturbances, the impacts of grid impedance, grid voltage distortion, and LVRT on the performance of the proposed method are evaluated. The experiment verifies the improvements in the system robustness using DDPB-PSMPC.

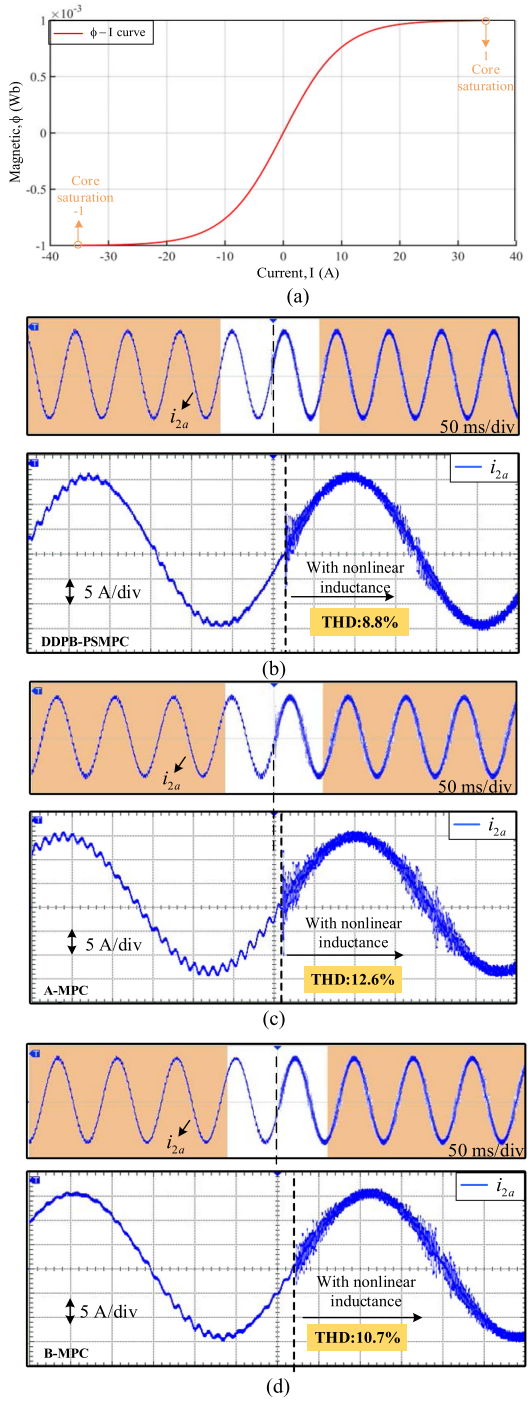

Fig. 13. Grid current with nonlinear inductance. (a) Magnetic flux versus current. (b) DDPB-PSMPC. (c) A-MPC. (d) B-MPC.

Fig. 14 shows the tracking performance of the grid current when an additional grid inductance L_g is added to *LCL*-3LT^{2}C. When $L_g = 8$ mH, the THD of the grid current with the DDPB-PSMPC, A-MPC, and B-MPC methods are reduced. The disturbance intensified when the grid inductance increased to 20 mH. After the transient-state process, the THD of the grid current with DDPB-PSMPC is 0.98%, which is 0.14% higher than that before grid inductance changes. The THD of the grid current

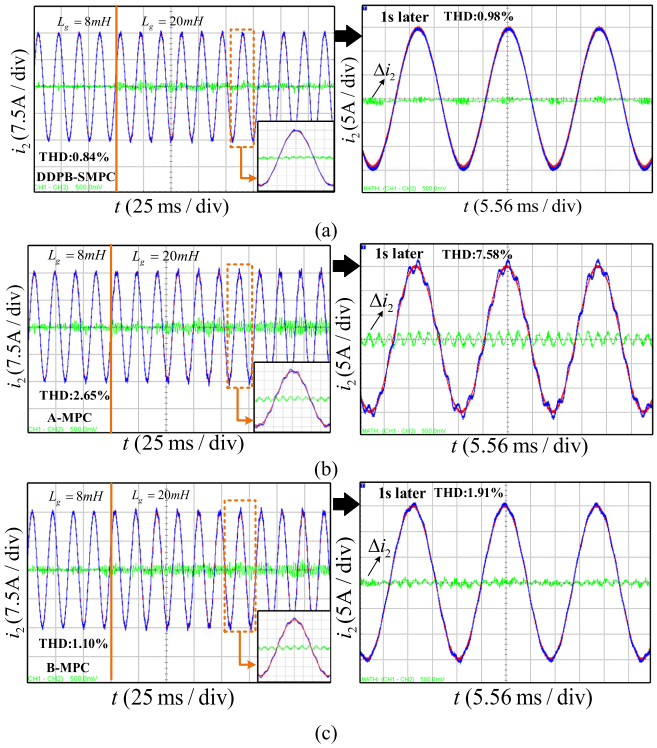

Fig. 14. Grid current with an increase of grid inductance. (a) DDPB-PSMPC. (b) A-MPC. (c) B-MPC.

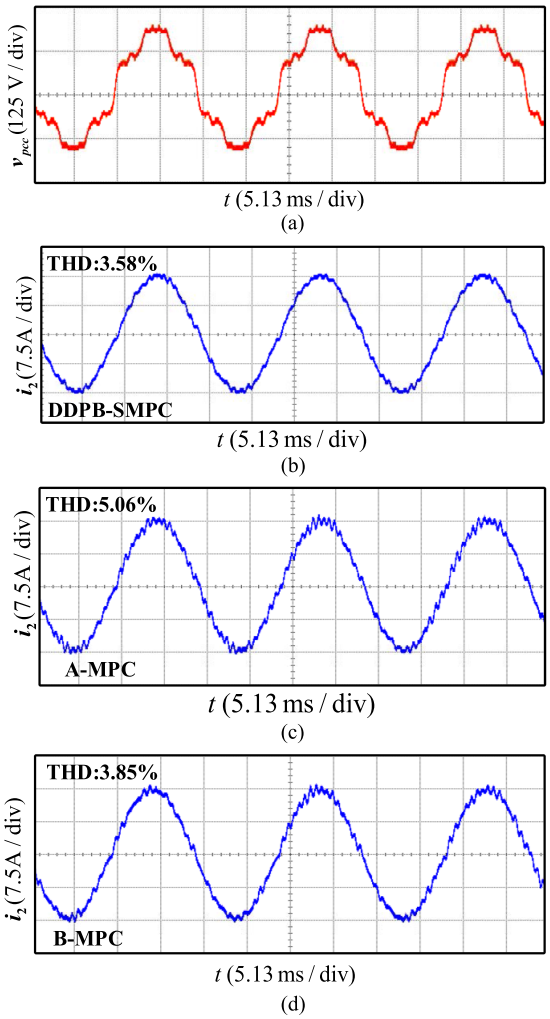

Fig. 15. Grid current under distorted grid voltage. (a) Distorted grid voltage. (b) DDPB-PSMPC. (c) A-MPC. (d) B-MPC.

with A-MPC increased to 3.41%, while that with B-MPC increased from 1.10% to 1.91%. For both methods, the waveforms are obviously distorted. This shows that the DDPB-PSMPC is more robust under grid impedance variations.

b) Distorted grid voltage: The grid voltage v_{pcc} can be distorted when the $3L^2TC$ is connected to the grid. The performances of the three control methods under a distorted grid voltage is tested. In Fig. 15(a), different harmonics (5th, 7th, 11th, 13th, and 23rd) are injected into the grid by a grid emulator. As shown in Fig. 15(b)–(d), the THD of grid current under DDPB-PSMPC, A-MPC, and B-MPC are 3.58%, 5.06%, and 3.85%, respectively. Compared to both conventional methods, DDPB-PSMPC has a better power quality for grid currents under distorted grid voltage.

c) Grid current and voltage under LVRT: Fig. 16(a)–(c) show the grid current under LVRT. When the amplitude of the grid voltage drops by half, after a transient oscillation, as shown in Fig. 16(a), the grid current under DDPB-PSMPC is stabilized. However, under A-MPC method in Fig. 16(b), LVRT shocks the grid current fiercely, there are several periodical oscillations. As shown in Fig. 16(c), two oscillations are observed for B-MPC and slight fluctuations accompanies the grid current when it enters a stable state. The results show that DDPB-PSMPC has good LVRT capability and has an excellent anti-disturbance ability.

Fig. 17 shows the waveforms of the grid voltage and current in *abc*-frame under LVRT using grid emulator Chroma 61800. With DDPB-PSMPC, after a short period of adjustment, the grid current is stabilized without additional harmonics. However, when LVRT occurs, the current harmonics under A-MPC control increase significantly (about 7.68%), because the disturbance injects to $3LT^2C$ cannot be eliminated in time. Oscillation of the grid current will continue. With B-MPC controller, the grid harmonic is lower than that of A-MPC, but still higher (about 2.61%) than that of DDPB-PSMPC (about 1.04%).

In summary, the proposed DDPB-PSMPC controller exhibits better robustness under LVRT, this also demonstrates its advantages over existing methods.

d) Unbalanced grid: Fig. 18 shows the waveforms of the grid current under unbalanced grid. The unbalanced degree of the grid is 30% (the unbalanced grid condition is realized by Chroma 61800). The effective values of the three-phase grid voltage V_{ga}, V_{gb}, and V_{gc} are about 110, 143, and 77 V. The grid currents with DDPB-PSMPC, A-MPC, and B-MPC controllers are shown as Fig. 18(b), (c), and (d), respectively. The results indicate that THD of the grid current is 2.40% when DDPB-PSMPC is applied, which is the lowest among three

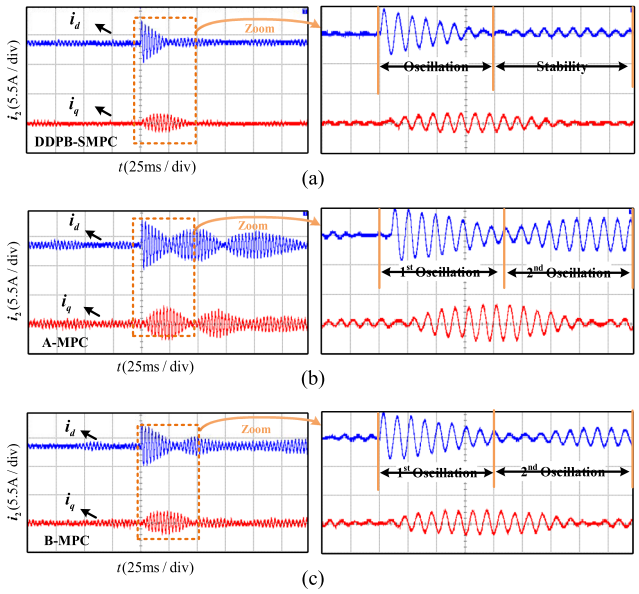

Fig. 16. Grid current in *dq*-frame under LVRT. (a) DDPB-PSMPC. (b) A-MPC. (c) B-MPC.

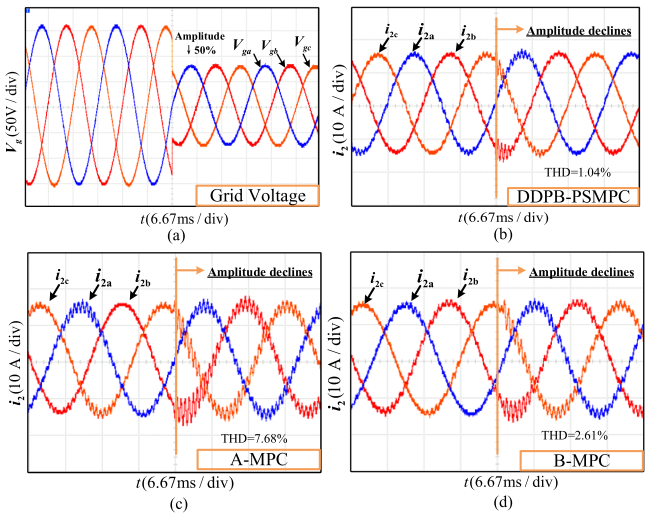

Fig. 17. Grid voltage and current in *abc*-frame under LVRT. (a) Grid voltage. (b) DDPB-PSMPC. (c) A-MPC. (d) B-MPC.

methods while that with A-MPC and B-MPC are 3.06% and 2.90%, respectively. This also demonstrates the advantage of the proposed method over existing controllers.

D. Summary

The performance of *LCL*-3LT^{2}C under DDPB-PSMPC, A-MPC, and B-MPC is evaluated under internal disturbances (e.g., filter parameter variations) and external disturbances (e.g., LVRT, unbalanced grid, weak grid, etc.). Summarily, although the A-MPC is simple, it has the worst robustness, and which

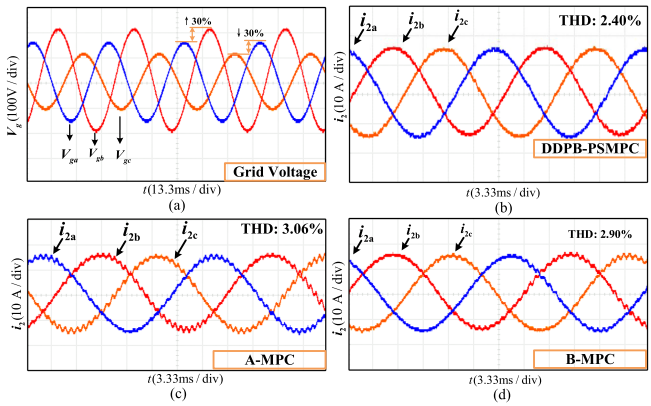

Fig. 18. Grid voltages and currents in abc-frame under unbalanced grid. (a) Grid voltage. (b) DDPB-PSMPC. (c) A-MPC. (d) B-MPC.

is sensitive to disturbances. Compared to B-MPC, the DDPB-PSMPC method reduces the control variable. Notably, DDPB-PSMPC is more robust to system parameter variations and disturbances.

VII. Conclusion

In this study, a DDPB-PSMPC is proposed to suppress the resonance and improve the anti-disturbance strength of *LCL*-3LT^{2}C when connected to a grid. According to the prediction error of the converter-side current, the DDPB-PSMPC injects dynamic damping into the PBC and the output voltage of the PBC controller is sent to the PSMPC controller as the reference. By tracking the PBC-voltage in PSMPC, the robustness of the *LCL*-3LT^{2}C system is strengthened and its resonance phenomenon is successfully suppressed. In addition, aiming at the time-consuming task to determine the optimal weighting factors in traditional MPC, DDPB-PSMPC allocates nonconflictive objectives in the same layer, thereby reducing the number of weighting factors and improving the system performance. The experiment compares DDPB-PSMPC to two existing traditional methods under internal and external disturbances and the results reveals that DDPB-PSMPC could effectively suppress resonance. Compared to $i_1 v_c i_2 \Delta v_{np}$-MPC, DDPB-PSMPC not only reduces the control objectives but increases the comprehensive anti-disturbance capability. The DDPB-PSMPC provides a new robust control for disturbances that could be applied to other GCCs.

References

[1] M. Narimani and G. Moschopoulos, "An investigation on the novel use of high-power three-level converter topologies to improve light-load efficiency in low power DC/DC full-bridge converters," *IEEE Trans. Ind. Electron.,* vol. 61, no. 10, pp. 5690–5692, Oct. 2014.

[2] D. Karwatzki and A. Mertens, "Generalized control approach for a class of modular multilevel converter topologies," *IEEE Trans. Power Electron.,* vol. 33, no. 4, pp. 2888–2900, Apr. 2018.

[3] P. Alemi, Y.-C. Jeung, and D.-C. Lee, "DC-link capacitance minimization in T-type three-level AC/DC/AC PWM converters," *IEEE Trans. Ind. Electron.,* vol. 62, no. 3, pp. 1382–1391, Mar. 2015.

[4] M. Schweizer and J. W. Kolar, "Design and implementation of a highly efficient three-level T-type converter for low-voltage applications," *IEEE Trans. Power Electron.,* vol. 28, no. 2, pp. 899–907, Feb. 2013.

[5] M. B. Saïd-Romdhane, M. W. Naouar, I. Slama-Belkhodja, and E. Monmasson, "Robust active damping methods for LCL filter-based grid-connected converters," *IEEE Trans. Power Electron.,* vol. 32, no. 9, pp. 6739–6750, Sep. 2017.

[6] B. I. Crăciun, T. Kerekes, D. Séra, and R. Teodorescu, "Overview of recent grid codes for PV power integration," in *Proc. 13th Int. Conf. Optim. Elect. Electron. Equip.*, 2012, pp. 959–965, doi: 10.1109/OPTIM.2012.6231767.

[7] E. Rodriguez-Diaz, F. D. Freijedo, J. C. Vasquez, and J. M. Guerrero, "Analysis and comparison of notch filter and capacitor voltage feedforward active damping techniques for LCL grid-connected converters," *IEEE Trans. Power Electron.,* vol. 34, no. 4, pp. 3958–3972, Apr. 2019.

[8] Y. Tang, W. Yao, P. C. Loh, and F. Blaabjerg, "Design of LCL filters with LCL resonance frequencies beyond the Nyquist frequency for grid-connected converters," *IEEE J. Emerg. Sel. Topics Power Electron.*, vol. 4, no. 1, pp. 3–14, Mar. 2016.

[9] A. Kouchaki and M. Nymand, "Analytical design of passive LCL filter for three-phase two-level power factor correction rectifiers," *IEEE Trans. Power Electron.,* vol. 33, no. 4, pp. 3012–3022, Apr. 2018.

[10] B. Long et al., "Noninteger lexicographic-optimization-based sequential model-predictive fault-tolerant control of T-type shunt active power filter," *IEEE Trans. Power Electron.,* vol. 37, no. 6, pp. 7169–7184, Jun. 2022.

[11] A. Ghoshal and V. John, "Active damping of LCL filter at low switching to resonance frequency ratio," *IET Power Electron.,* vol. 8, no. 4, pp. 574–582, Apr. 2015, doi: 10.1049/iet-pel.2014.0355.

[12] L. Zhou et al., "Inverter-current-feedback resonance-suppression method for *LCL*-type DG system to reduce resonance-frequency offset and grid-inductance effect," *IEEE Trans. Ind. Electron.,* vol. 65, no. 9, pp. 7036–7048, Sep. 2018.

[13] H.-C. Chen, P.-T. Cheng, X. Wang, and F. Blaabjerg, "A passivity-based stability analysis of the active damping technique in the offshore wind farm applications," *IEEE Trans. Ind. Appl.,* vol. 54, no. 5, pp. 5074–5082, Sep./Oct. 2018.

[14] S. Vazquez, J. Rodriguez, M. Rivera, L. G. Franquelo, and M. Norambuena, "Model predictive control for power converters and drives: Advances and trends," *IEEE Trans. Ind. Electron.,* vol. 64, no. 2, pp. 935–947, Feb. 2017.

[15] S. Vazquez et al., "Model predictive control: A review of its applications in power electronics," *IEEE Ind. Electron. Mag.,* vol. 8, no. 1, pp. 16–31, Mar. 2014.

[16] H. A. Young, M. A. Perez, and J. Rodriguez, "Analysis of finite-control-set model predictive current control with model parameter mismatch in a three-phase inverter," *IEEE Trans. Ind. Electron.,* vol. 63, no. 5, pp. 3100–3107, May 2016.

[17] X. Zhang, X. Wu, G. Tan, W. Zhang, and Q. Wang, "A dual-vector model predictive control method with minimum current THD," *IEEE Trans. Power Electron.,* vol. 36, no. 9, pp. 9758–9762, Sep. 2021.

[18] T. Liu, A. Chen, F. Gao, X. Liu, X. Li, and S. Hu, "Double-loop control strategy with cascaded model predictive control to improve frequency regulation for islanded microgrids," *IEEE Trans. Smart Grid*, vol. 13, no. 5, pp. 3954–3967, Sep. 2022.

[19] P. Falkowski and A. Sikorski, "Finite control set model predictive control for grid-connected AC–DC converters with LCL filter," *IEEE Trans. Ind. Electron.,* vol. 65, no. 4, pp. 2844–2852, Apr. 2018.

[20] C. Xue, D. Zhou, and Y. Li, "Hybrid model predictive current and voltage control for *LCL*-filtered grid-connected inverter," *IEEE J. Emerg. Sel. Topics Power Electron.,* vol. 9, no. 5, pp. 5747–5760, Oct. 2021.

[21] N. Panten, N. Hoffmann, and F. W. Fuchs, "Finite control set model predictive current control for grid-connected voltage-source converters with LCL filters: A study based on different state feedbacks," *IEEE Trans. Power Electron.,* vol. 31, no. 7, pp. 5189–5200, Jul. 2016.

[22] H. Liao, X. Zhang, and Z. Ma, "Robust dichotomy solution-based model predictive control for the grid-connected inverters with disturbance observer," *CES Trans. Elect. Machines Syst.,* vol. 5, no. 2, pp. 81–89, 2021, doi: 10.30941/CESTEMS.2021.00011.

[23] Z. Song, Y. Tian, Z. Yan, and Z. Chen, "Direct power control for three-phase two-level voltage-source rectifiers based on extended-state observation," *IEEE Trans. Ind. Electron.,* vol. 63, no. 7, pp. 4593–4603, Jul. 2016.

[24] Z. Song, C. Xia, and T. Liu, "Predictive current control of three-phase grid-connected converters with constant switching frequency for wind energy systems," *IEEE Trans. Ind. Electron.,* vol. 60, no. 6, pp. 2451–2464, Jun. 2013.

[25] F. Wang, D. Ke, X. Yu, and D. Huang, "Enhanced predictive model based deadbeat control for PMSM drives using exponential extended state observer," *IEEE Trans. Ind. Electron.,* vol. 69, no. 3, pp. 2357–2369, Mar. 2022.

[26] L. Yan, F. Wang, M. Dou, Z. Zhang, R. Kennel, and J. Rodríguez, "Active disturbance-rejection-based speed control in model predictive control for induction machines," *IEEE Trans. Ind. Electron.,* vol. 67, no. 4, pp. 2574–2584, Apr. 2020.

[27] M. S. Mousavi, S. A. Davari, V. Nekoukar, C. Garcia, and J. Rodriguez, "A robust torque and flux prediction model by a modified disturbance rejection method for finite-set model-predictive control of induction motor," *IEEE Trans. Power Electron.,* vol. 36, no. 8, pp. 9322–9333, Aug. 2021.

[28] N. Guler, S. Biricik, S. Bayhan, and H. Komurcugil, "Model predictive control of DC–DC SEPIC converters with autotuning weighting factor," *IEEE Trans. Ind. Electron.,* vol. 68, no. 10, pp. 9433–9443, Oct. 2021.

[29] T. Dragicevic and M. Novak, "Weighting factor design in model predictive control of power electronic converters: An artificial neural network approach," *IEEE Trans. Ind. Electron.,* vol. 66, no. 11, pp. 8870–8880, Nov. 2019.

[30] Y. Yang, H. Wen, M. Fan, M. Xie, and R. Chen, "Fast finite-switching-state model predictive control method without weighting factors for T-type three-level three-phase inverters," *IEEE Trans. Ind. Informat.,* vol. 15, no. 3, pp. 1298–1310, Mar. 2019.

[31] M. Norambuena, J. Rodriguez, Z. Zhang, F. Wang, C. Garcia, and R. Kennel, "A very simple strategy for high-quality performance of AC machines using model predictive control," *IEEE Trans. Power Electron.,* vol. 34, no. 1, pp. 794–800, Jan. 2019.

[32] P. Karamanakos and T. Geyer, "Guidelines for the design of finite control set model predictive controllers," *IEEE Trans. Power Electron.,* vol. 35, no. 7, pp. 7434–7450, Jul. 2020.

[33] Y. Jiang, C. Qin, X. Xing, X. Li, and C. Zhang, "A hybrid passivity-based control strategy for three-level T-type inverter in LVRT operation," *IEEE J. Emerg. Sel. Topics Power Electron.,* vol. 8, no. 4, pp. 4009–4024, Dec. 2020.

[34] J. Zhao, C. Xie, K. Li, J. Zou, and J. M. Guerrero, "Passivity-oriented design of *LCL*-type grid-connected inverters with luenberger observer-based active damping," *IEEE Trans. Power Electron.,* vol. 37, no. 3, pp. 2625–2635, Mar. 2022.

[35] Y. X. Liu et al., "Passivity-based decoupling control strategy of single-phase *LCL*-type VSRs for harmonics suppression in railway power systems," *Int. J. Elect. Power Energy Syst.,* vol. 117, May 2020, Art no. 105698, doi: 10.1016/j.ijepes.2019.105698.

[36] J. Wang, X. Mu, and Q.-K. Li, "Study of passivity-based decoupling control of T-NPC PV grid-connected inverter," *IEEE Trans. Ind. Electron.,* vol. 64, no. 9, pp. 7542–7551, Sep. 2017.

[37] S. Sternberg, *Dynamical Systems*. Chelmsford, MA, USA: Courier Corporation, 2010.

[38] F. Wang, G. Lin, and Y. He, "Passivity-based model predictive control of three-level inverter-fed induction motor," *IEEE Trans. Power Electron.,* vol. 36, no. 2, pp. 1984–1993, Feb. 2021.

[39] Y. Tang, P. C. Loh, P. Wang, F. H. Choo, F. Gao, and F. Blaabjerg, "Generalized design of high performance shunt active power filter with output LCL filter," *IEEE Trans. Ind. Electron.,* vol. 59, no. 3, pp. 1443–1452, Mar. 2012.

[40] J. Xu, S. Xie, and T. Tang, "Systematic current control strategy with pole assignment for grid-connected *LCL*-filtered inverters," *J. Power Electron.,* vol. 13, no. 3, pp. 447–457, 2013, doi: 10.6113/JPE.2013.13.3.447.

[41] T. Ding and A. Hirose, "Fading channel prediction based on combination of complex-valued neural networks and chirp Z-transform," *IEEE Trans. Neural Netw. Learn. Syst.,* vol. 25, no. 9, pp. 1686–1695, Sep. 2014.

[42] B. Long, T. Cao, D. Sheng, J. Rodriguez, J. M. Guerrero, and K. T. Chong, "Sequential model predictive fault-tolerance control for T-type three-level grid-connected converters with LCL filters," *IEEE Trans. Ind. Electron.,* vol. 69, no. 9, pp. 9039–9051, Sep. 2022.

[43] Y. Jiao and F. C. Lee, "LCL filter design and inductor current ripple analysis for a three-level NPC grid interface converter," *IEEE Trans. Power Electron.,* vol. 30, no. 9, pp. 4659–4668, Sep. 2015.

[44] D.-P. Xu, Y.-W. Jiang, and S.-M. Hwang, "Analysis of the magnetization effect of permanent magnets on the nonlinear magnetic characteristic distributions of a balanced armature receiver," *IEEE Trans. Magn.,* vol. 55, no. 2, Feb. 2019, Art. no. 8200305.

[45] D. Xiao, J. Ye, G. Fang, Z. Xia, and A. Emadi, "Magnetic-characteristic-free high-speed position-sensorless control of switched reluctance motor drives with quadrature flux estimators," *IEEE J. Emerg. Sel. Topics Power Electron.,* vol. 10, no. 1, pp. 220–235, Feb. 2022.

Bo Long (Senior Member, IEEE) received the B.S. degree from the Xi'an Petroleum University, Xian, China, in 2001, and the Ph.D. degree from Xian Jiaotong University, Shanxi, China, in 2008, both in electrical engineering.

From 2017 to 2018, he was a Visiting Scholar (Guest Postdoctoral Researcher) in renewable energy and microgrids with the Department of Electrical Engineering, Tsinghua University, Beijing, China. He joined the Department of Power Electronics, School of Mechatronics Engineering, University of Electronic Science and Technology of China, Chengdu, China, in 2008, and has been promoted to an Associate Professor since 2014. His research interests include ac/dc microgrids, grid-connected converters for renewable energy systems and DGs, model predictive control, power quality, multilevel converters, ac motor control, and resonance suppression technique for smart grid applications. He has authored more than 20 SCIE-indexed journal papers and 1 book chapter in power electronics, motor control, battery management system, and smart grid. He has 7 issued and 10 pending patents. He is currently the Supervisor for 11 master students, 2 of which have been nominated as provincial outstanding graduate student of UESTC.

DaWei Shen received the B.S. degree in smart grid information engineering from Nanjing University of Posts and Telecommunications, Nanjing, China, in 2019. He is currently working toward the M.S. degree in mechanical engineering from University of Electronic Science and Technology of China, Chengdu, China.

His current research interest includes model predictive control of power converters, passive-based control, power loss minimization of power converters, microgrids system, and so on.

TianXu Cao received the B.S. degree in electrical engineering in 2020 from the University of Electronic Science and Technology of China, Chengdu, China, where he is currently working toward the M.S. degree in mechanical engineering.

His current research interests include the optimization of direct microgrids, involving virtual inertia control, fault-tolerant control of power converters, model predictive control, fractional-order systems, reliability of power electronic system, and so on.

Jose Rodriguez (Fellow, IEEE) received the Engineer's degree in electrical engineering from the Universidad Tecnica Federico Santa Maria, Valparaiso, Chile, in 1977, and the Dr.-Ing. degree in electrical engineering from the University of Erlangen, Erlangen, Germany, in 1985.

He has been with the Department of Electronics Engineering, Universidad Tecnica Federico Santa Maria, since 1977, where he was a Full Professor and President. Since 2015 he has been the President of Universidad Andres Bello, Santiago, Chile. He has coauthored 2 books, several book chapters, and more than 400 journal and conference papers. His main research interests include multilevel inverters, new converter topologies, control of power converters, and adjustable-speed drives.

Dr. Rodriguez was the recipient of several best paper awards from journals of the IEEE, the National Award of Applied Sciences and Technology from the government of Chile, in 2014 and the Eugene Mittelmann Award from the Industrial Electronics Society of the IEEE, in 2015. He is a member of the Chilean Academy of Engineering

Josep M. Guerrero (Fellow, IEEE) received the B.S. degree in telecommunications engineering, the M.S. degree in electronics engineering, and the Ph.D. degree in power electronics from the Technical University of Catalonia, Catalonia, Barcelona, in 1997, 2000 and 2003, respectively.

Since 2011, he has been a Full Professor with the Department of Energy Technology, Aalborg University, Denmark, where he is responsible for the Microgrid Research Program. In 2014, he was a Chair Professor with Shandong University; in 2015 a distinguished Guest Professor with Hunan University; and in 2016 a Visiting Professor Fellow with Aston University, U.K., and a Guest Professor with the Nanjing University of Posts and Telecommunications. In 2019, he became a Villum Investigator by The Villum Fonden, which supports the Center for Research on Microgrids (CROM) at Aalborg University, being Prof. Guerrero the founder and Director of the same center (www.crom.et.aau.dk). He has authored and coauthored more than 600 journal papers in the fields of microgrids and renewable energy systems, which are cited more than 50000 times. His research interests include different microgrid aspects, including power electronics, distributed energy-storage systems, hierarchical and cooperative control, energy management systems, smart metering and the internet of things for ac/dc microgrid clusters and islanded microgrids. Specially focused on microgrid technologies applied to offshore wind, maritime microgrids for electrical ships, vessels, ferries and seaports, and space microgrids applied to nanosatellites and spacecrafts.

Dr. Guerrero was the recipient of the best paper award of the IEEE Transactions on Energy Conversion for the period 2014–2015, and the best paper prize of IEEE-PES, in 2015, and the best paper award of the Journal of Power Electronics in 2016. From 2014 to 2019, he was awarded by Clarivate Analytics (former Thomson Reuters) as Highly Cited Researcher with 50 highly cited papers. He is an Associate Editor for several IEEE TRANSACTIONS.

Kil To Chong (Member, IEEE) received the Ph.D. degree in mechanical engineering from Texas A&M University, College Station, TX, USA, in 1995.

He is currently a Professor and the Department Head with the School of Electronics and Information Engineering and a member and the Head of the Advanced Electronics and Information Research Center, Chonbuk National University, Jeonju, South Korea. His research interests include motor fault detection and control, network system control, sensor network systems, time-delay systems, and neural networks.

YunLong Teng received the Ph.D. degree in measurement technology and instrument from the University of Electronic Science and Technology of China (UESTC), Chengdu, China, in 2011.

He is currently an Associate Professor with the School of Mechanical and Electrical Engineering, UESTC. His research interests include wide-area measurement, sliding mode control, and control on renewable power generation systems.